14. The Genesis Problem

No aspect of tropical cyclones has proved more challenging than their genesis. After decades of research, there is little consensus on how tropical cyclone form, and our ability to forecast whether a particular cloud cluster or easterly wave will develop remains rudimentary. The one statistic we can forecast nearly perfectly is the global, annual number of storms which, as demonstrated in Figure 14.1, is remarkably stable at about 90. The interannual standard deviation is 9.5, very close to the square root of the mean as would be expected in pure Poisson variability. There is no significant long-term trend.

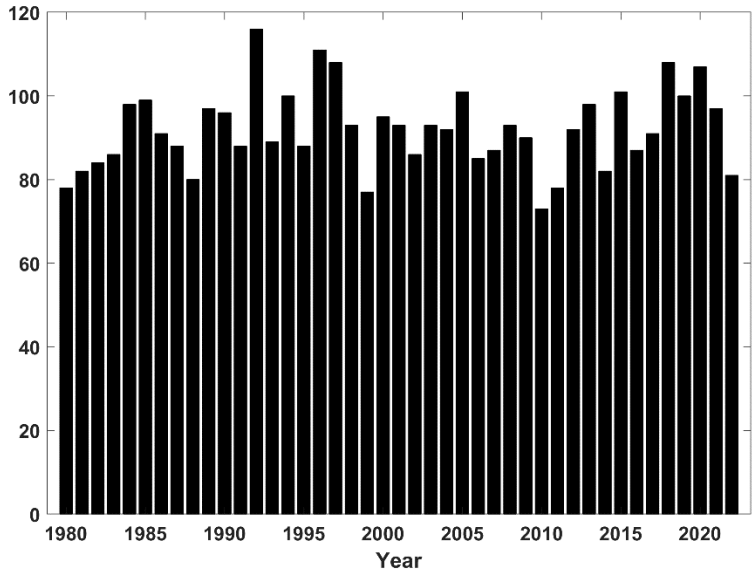

Figure 14.1: Annual, global number of tropical cyclones in the IBTrACS data set (Knapp et al. 2010), from 1980 through 2022. Only cyclones whose lifetime maximum surface winds reach at least 35 knots (18 ms^{-1}) are included. The long-term mean is 92 with a standard deviation of 9.5. Global tropical cyclone counts prior to about 1980 are compromised by poor or nonexistent satellite coverage.

At the time of this writing, there is no generally accepted theory for why there are O(100) tropical cyclones on our planet each year or why that number is so stable in spite of large inter-basin and seasonal variability.

Historically, there have been two threads of research on genesis. The first, which we here label the “local view”, focuses on how individual tropical cyclones come about, using observations and models. Early in the post-WWII renaissance of tropical cyclone research, it was recognized that most if not all tropical cyclones originate from independent disturbances such as African easterly waves (Dunn 1940; Riehl 1948a,b; Dunn 1951; Riehl 1951; Ramage 1959; Riehl 1975). Much research effort has been expended on whether and how such independent disturbances transform into tropical cyclones, partly to support efforts to forecast genesis in real time.

The second thread, begun by Palmén (1948) and expanded on by Gray (1975, 1979), focuses on susceptibility of the large-scale thermodynamic and kinematic environment to genesis. We label this thread the “global view”.

In this chapter, we will look at genesis through both of these lenses and attempt a synthesis that may help explain both how tropical cyclones develop and what controls their overall climatology.

14.1 The local view

We begin by looking at a strongly developing and a non-developing tropical Atlantic wave disturbance and see how they fit in with previous observational and field experimental inferences. We then proceed to a theoretical interpretation of these observations and conclude this section with a synthesis of the local view.

14.1.1 Case study: The development of Hurricane Ivan of 2004

Here we examine a particular case of tropical cyclogenesis that took place in the North Atlantic, leading to Hurricane Ivan of 2004. Figure 14.2 shows the track and maximum wind speeds in Hurricane Ivan.

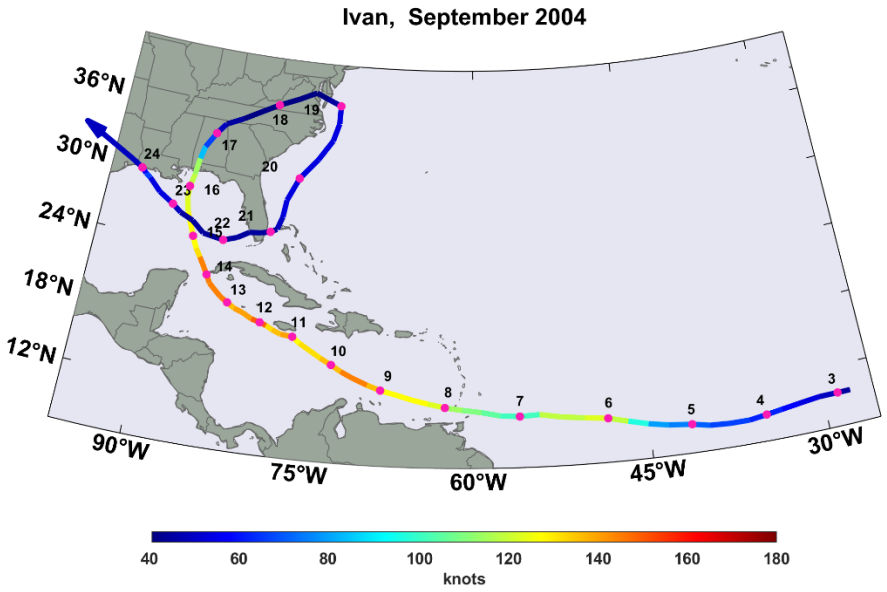

Figure 14.2: Track of the center of Hurricane Ivan of 2004. Numbers correspond to 00 GMT dates in September. Colors signify maximum wind speeds (kts).

Ivan followed a classical evolution into a "Cape Verde" hurricane from an easterly wave that moved off the west coast of Africa on August 31st. Its track after landfall in Alabama and the Florida panhandle was, however, unusual. We will focus on its development from September 1st to September 5th. Figure 14.3 shows pre-Ivan's evolution in 4 snapshots during this time period.

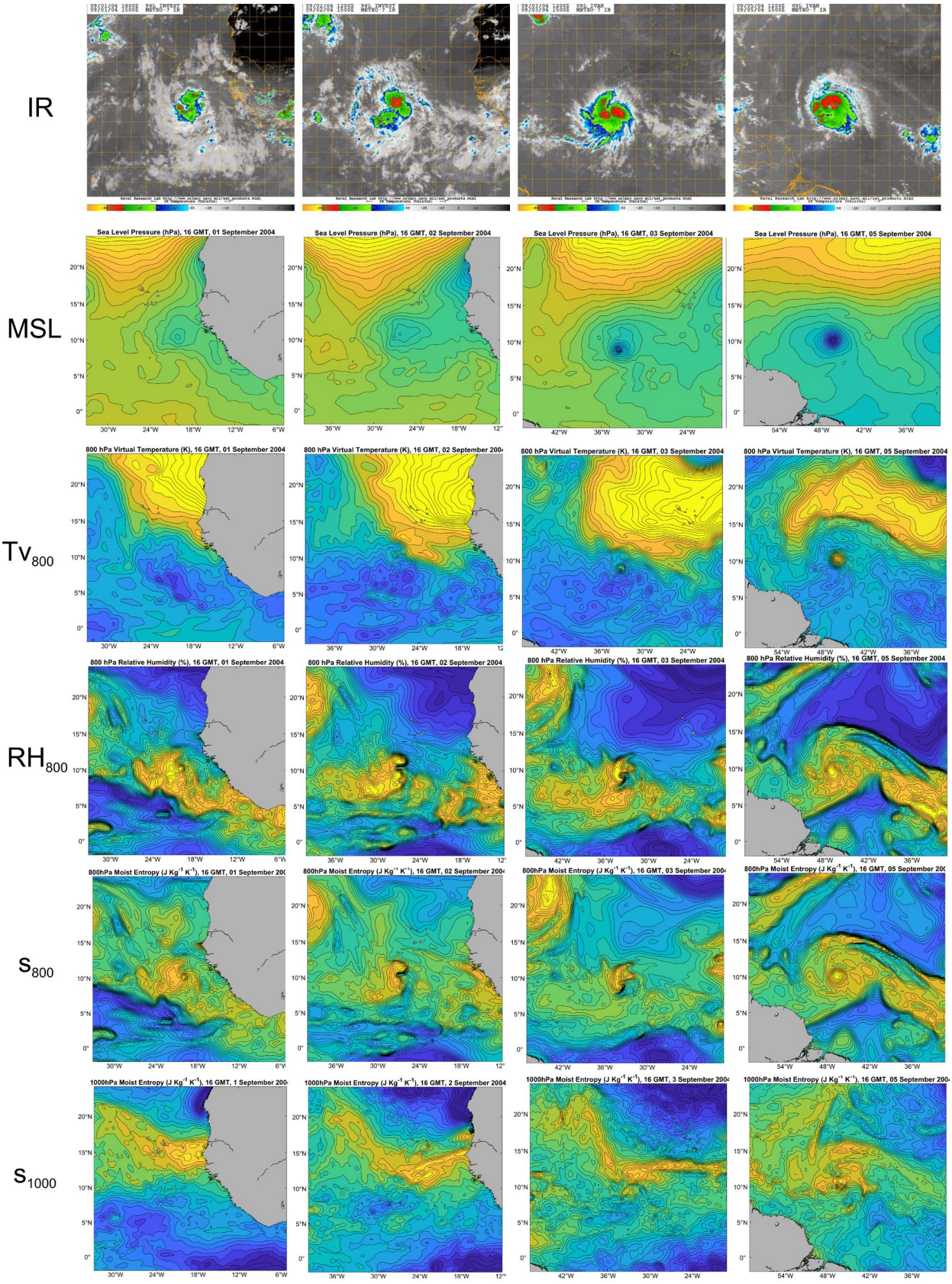
IR
MSL
Tv800
RH800
s800
s1000
Sea Level Pressure (hPa), 16 GMT, 01 September 2004
Sea Level Pressure (hPa), 16 GMT, 02 September 2004
Sea Level Pressure (hPa), 16 GMT, 03 September 2004
Sea Level Pressure (hPa), 16 GMT, 05 September 2004
800 hPa Virtual Temperature (K), 16 GMT, 01 September 2004
800 hPa Virtual Temperature (K), 16 GMT, 02 September 2004
800 hPa Virtual Temperature (K), 16 GMT, 03 September 2004
800 hPa Virtual Temperature (K), 16 GMT, 05 September 2004
800 hPa Relative Humidity (%), 16 GMT, 01 September 2004
800 hPa Relative Humidity (%), 16 GMT, 02 September 2004
800 hPa Relative Humidity (%), 16 GMT, 03 September 2004
800 hPa Relative Humidity (%), 16 GMT, 05 September 2004
800hPa Moist Entropy (J Kg-1 K-1), 16 GMT, 01 September 200
800hPa Moist Entropy (J Kg-1 K-1), 16 GMT, 02 September 2004
800hPa Moist Entropy (J Kg-1 K-1), 16 GMT, 03 September 2004
800hPa Moist Entropy (J Kg-1 K-1), 16 GMT, 05 September 200
1000hPa Moist Entropy (J Kg-1 K-1), 16 GMT, 1 September 200
1000hPa Moist Entropy (J Kg-1 K-1), 16 GMT, 2 September 2004
1000hPa Moist Entropy (J Kg-1 K-1), 16 GMT, 3 September 200
1000hPa Moist Entropy (J Kg-1 K-1), 16 GMT, 05 September 200
September 1
September 2
September 3
September 5

Figure 14.3: Evolution of Ivan from September 1st to September 5th, 2004 at 16 GMT, skipping September 4th for space reasons. The top row shows storm-centered infrared imagery from the Geostationary Operational Environmental Satellite (GOES), while all the other rows display fields from ERA5 hourly reanalyses. From row 2 to row 6: Mean sea-level pressure (from 1002 to 1018 hPa), 800 hPa virtual temperature (from 287 to 293 K), 800 hPa relative humidity (from 20 to 100 %), 800 hPa moist entropy (from 5780 to 5870 J Kg^{-1} K^{-1}) and 1000 hPa moist entropy (from 5840 to 5890 J Kg^{-1} K^{-1}).

The top row shows infrared imagery from a geostationary satellite while the other rows show fields from the European center for Medium Range Forecasts Re-Analysis 5 (ERA5; Hersbach et al. 2020). The reanalysis is based on running a global, high-resolution weather forecast model while assimilating most available observations, including from satellites, aircraft, rawinsondes, and surface-based platforms. The imagery and the ERA5 fields are aligned in space and time and follow the cyclone from a tropical wave on September 1st to a tropical storm on September 5th.

In interpreting these fields, one must bear in mind that re-analyses are not observations. There are very few in-situ observations in the region covered, and one must rely on the model itself and its ability to assimilate what observations there are.

A loosely organized, roughly circular cloud cluster moves away from the African coast on September 1st. A broad, weak area of low pressure accompanies the cluster, and a stronger cyclone has developed within it by September 3rd. At 800 hPa, the core of this disturbance is cold and humid (third and fourth rows of Figure 14.3) and while it has elevated moist entropy at 800 hPa (fifth row), there is a depression in the boundary layer (1000 hPa) moist entropy for the first two days of the evolution shown. Not until September 3rd does a high entropy core begin to develop in the boundary layer. The lower tropospheric part of the disturbance remains cold but by September 5th a very small, intense warm core has developed, visible in the 800 hPa virtual temperature field. (The disturbance has a warm core in the upper troposphere (not shown) through the whole period.)

Note that the high moist entropy core at 1000 hPa evident on September 5th interacts with a thin strip of high moist entropy moving off the central African coastline. This strip is muted at 800 hPa but by September 5th a broad region of elevated entropy surrounds the tight, high-entropy core of Tropical Storm Ivan.

Another feature of possible relevance is the large plume of hot but dry air emanating from the Sahara Desert, as visible in the 800 hPa virtual temperature and relative humidity. The moist entropy of this air is not very different from that of the surrounding air mass. By September 5th it has started to wrap around the western periphery of Ivan. Otherwise, the fields delineating Ivan's core and immediate surrounds are beginning to resemble those of a mature tropical cyclone by this time.

14.1.2: Case study: The non-development of Tropical Storm Gaston of 2010

The disturbance that eventually became Gaston, as weak tropical storm, followed an initial trajectory similar to that of Ivan of 2004, as shown in Figure 14.4.

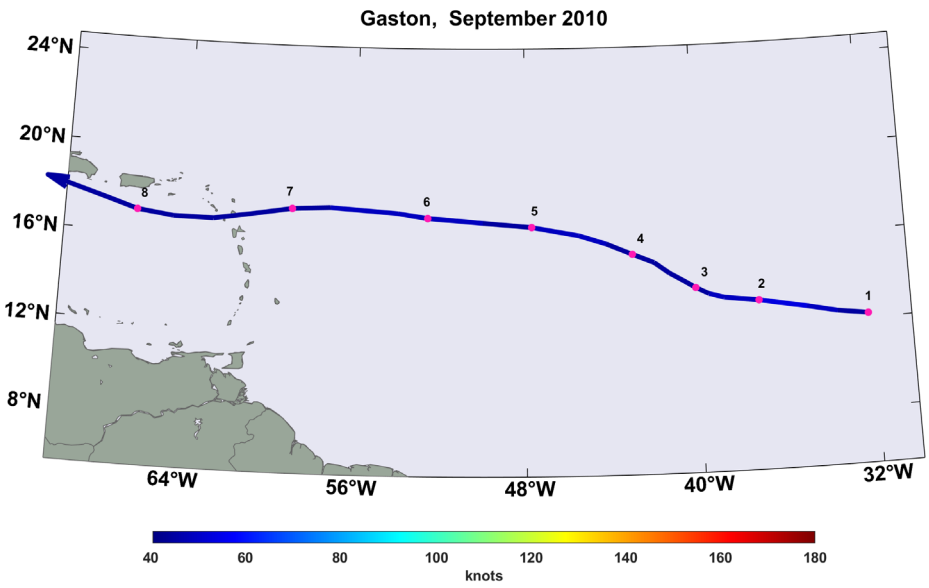

Figure 14.4: Track of Tropical Storm Gaston of 2010. As in Figure 14.2, the red dots denote the 00 GMT positions of the storm center at the September dates indicated by the numerals.

According to NOAA/National Hurricane Center records, Gaston's maximum winds peak at 35 knots (18 ms^{-1}) on September 2nd and 3rd and remained at or below 30 knots (15 ms^{-1}) thereafter.

Figure 14.5 shows the infrared presentation of Gaston, together with the virtual temperature and moist entropy at 800 hPa at three times. (Note the smaller scale of the maps in Figure 14.5 compared to Figure 14.3.) At 06 GMT on August 31st, an impressive cloud cluster is visible in the IR satellite image, but there is little indication of any disturbance at 800 hPa in either the ERA5 virtual temperature or moist entropy fields. (There is, however, a weak depression in sea level pressure, not shown here; co-located with a positive virtual temperature anomaly at 300 hPa.) The absence of a significant perturbation in the low-level thermodynamic fields suggests either that the cloud cluster does not yet have significant rotation or that the re-analysis has missed these features. Note the very hot Saharan air mass with a sharp southern boundary.

Several days later, at 00 GMT on September 3rd, the cloud cluster has almost disappeared from the infrared satellite image, yet by this time there are significant perturbations in the virtual temperature and moist entropy fields at 800 hPa. (It should be noted, though, that this is at about the local time of a diurnal minimum in moist convection over tropical oceans.) A negative virtual temperature anomaly has developed, apparently by virtue of Gaston's circulation penetrating the very hot Saharan airmass to its north, but a prominent positive moist entropy anomaly suggests that surface fluxes may be pumping high entropy into the lower troposphere. Also of interest is the band of high most entropy associated with the ITCZ to the south of Gaston. Sixty hours later, on September 5th, the cloud cluster appears to be re-intensifying (though note the opposite phase of the diurnal cycle from the previous image) and there are prominent positive anomalies in both virtual temperature and moist entropy at 800 hPa, more or less collocated with the cold cloud tops.

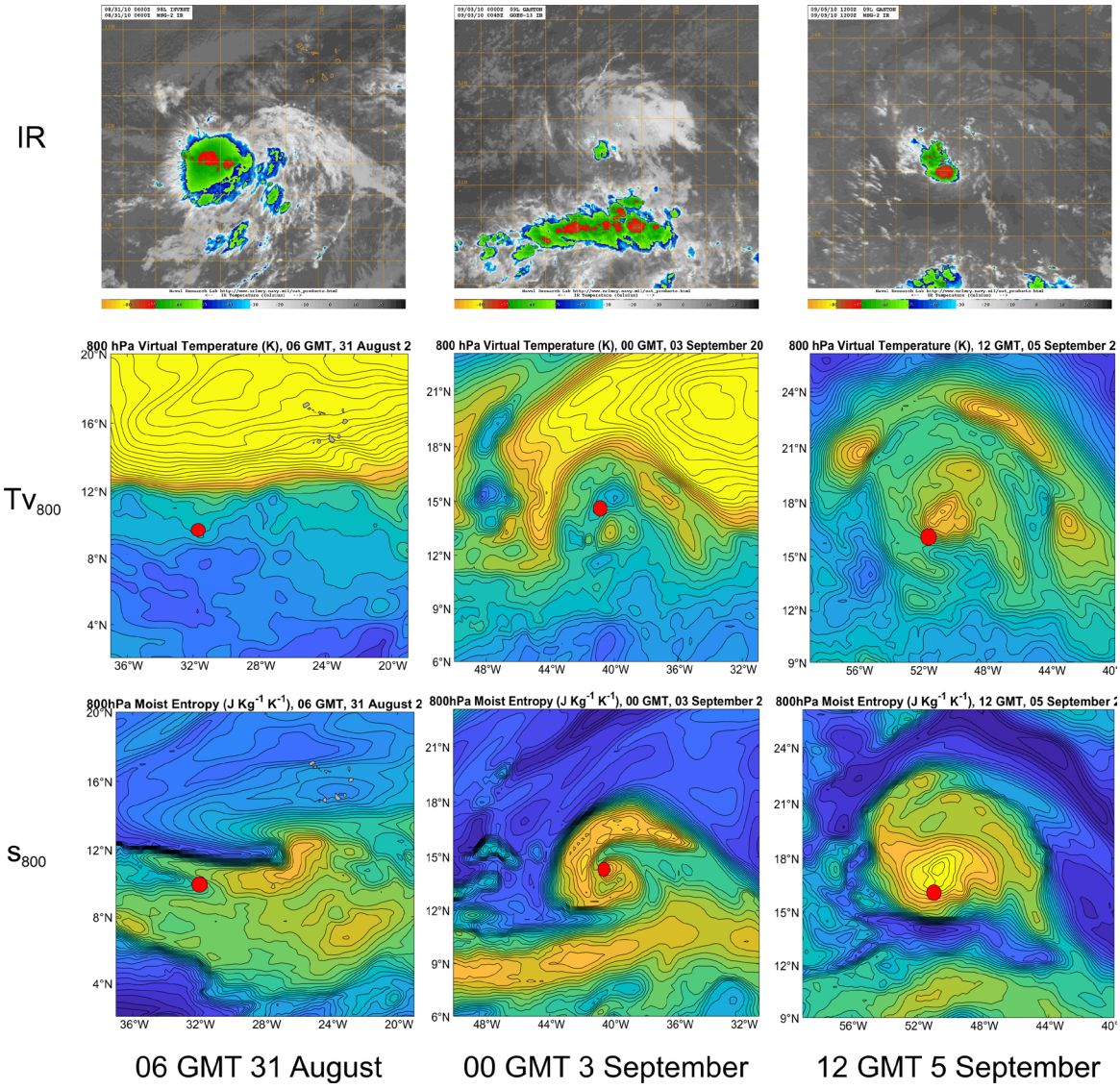

Figure 14.5: Evolution of Gaston from 06 GMT August 31st to 12 GMT September 5th, 2010. The top row shows storm-centered infrared imagery from the Geostationary Operational Environmental Satellite (GOES) while all the other rows display fields from ERA5 hourly reanalyses. Row 2: 800 hPa virtual temperature (from 287 to 293 K); Row 3: 800 hPa moist entropy (from 5790 to 5880 J Kg^{-1} K^{-1}). The red dot in the last two rows shows the approximate position of the IR temperature minimum (top row).

Comparing to Figure 14.3 for Ivan, and accounting for the different map scales (though the color scales span the same ranges), the low-level thermodynamic fields would seem to indicate a robustly intensifying system. But note that the warm core is not as concentrated as in the case of Ivan when it was of comparable age and strength. Moreover, according to the NOAA data, Gaston is weaker at this time than on September 3rd and never regained tropical storm intensity. What made the difference?

A clue to this enigma might be present in the relative humidity fields higher up, as shown in Figure 14.6, which compares the evolution of Hurricane Ivan of 2004 (top row) to that of Tropical Storm Gaston of 2010 (bottom row) in terms of the relative humidity at 600 hPa.

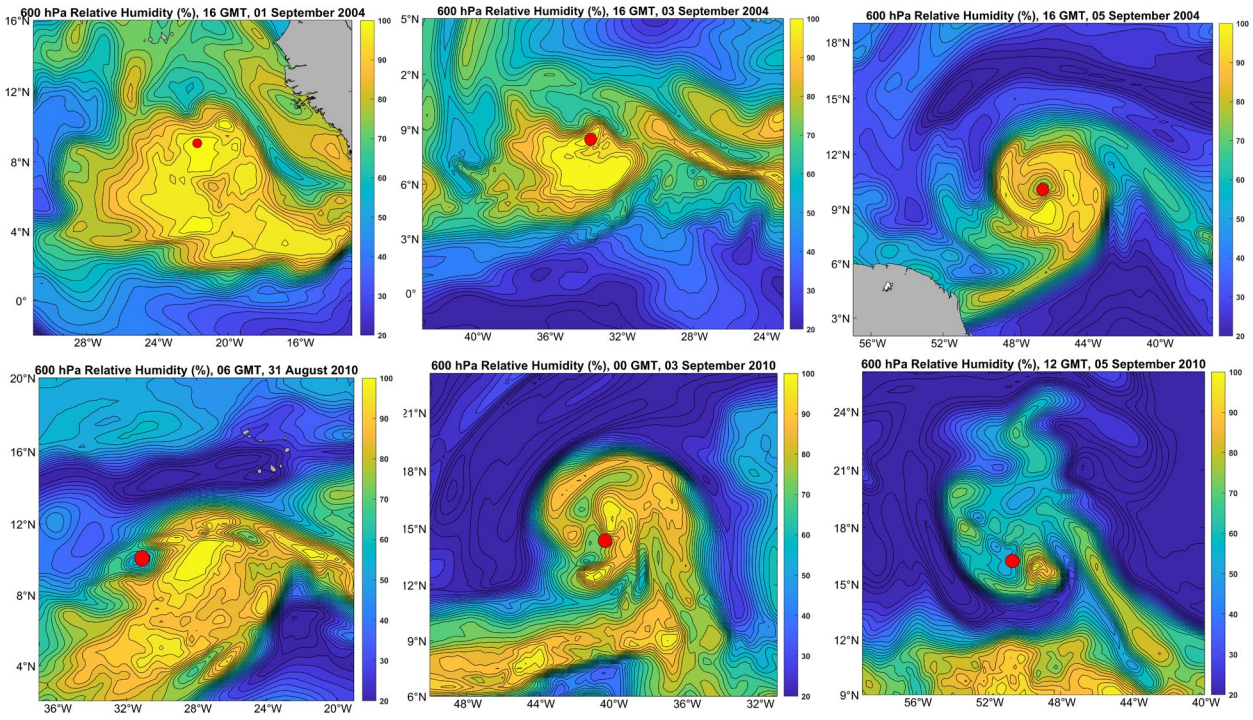

Figure 14.6: ERA5 relative humidity at 600 hPa during the development of Ivan of 2004 (top row) and Gaston of 2010 (bottom row). The Ivan sequence is for 16 GMT on September 1st, 3rd, and 5th, 2004 and the Gaston sequence is for 06 GMT on August 31st, 00 GMT on September 3rd and 12 GMT on September 5th, 2010. The red dot on each panel shows the approximate position of the coldest infrared cloud tops in each case. Note that an effort has been made to keep all of the maps at about the same scale, and the relative humidity color scale (20-100%) is identical across the maps.

Note that in Ivan's case, the 600 hPa relative humidity anomaly is closer to saturation and/or more closely aligned with the convection (as indicated by the cloud top temperature minimum), and in the last two columns, more coherent than was the case with Gaston. And while Gaston's 800 hPa moist entropy anomaly amplified between the second and third time periods (Figure 14.5), the 600 hPa relative humidity clearly dropped, along with the intensity.

A closer inspection of the bottom row of Figure 14.6 suggests that by September 3rd, dry air was beginning to wrap around the west side of Gaston, and by September 5th it had begun to wrap into the core of the system.

Now of course it is possible that the drying out of Gaston's core was an effect of its weakening rather than the cause, if all we have to go on is the observation of its drying out. Later in this chapter we will argue, on the grounds of theory and models, that the core drying is indeed key to understanding Gaston's demise and probably the non-development of most tropical disturbances.

14.1.3 Ivan and Gaston in the context of other observational studies and field programs

Hurricane Ivan of 2004 began life as a weak cyclonic disturbance with a distinct cold core in the lower troposphere, quite the opposite of what we expect and observe in mature tropical cyclones. This appears to be a common route to genesis. By the late 1940s, Riehl (1948a) had already noticed that most tropical cloud clusters have cold cores in the lower troposphere. We know that African easterly waves have maximum amplitude in the middle troposphere, around

600 hPa (see Chapter 7, section 7.3), and quasi-balance considerations dictate that the troposphere beneath this level must be anomalously cold. Analysis of aircraft, Doppler, and dropsonde data deployed into eastern North Pacific Hurricane Guillermo of 1991 showed a prominent lower tropospheric cold core with anticyclonic surface circulation, within which a smaller scale (relative) warm core cyclone developed and eventually became a hurricane (Bister and Emanuel 1997). The development of a small warm core within a broader cold core was quite similar to the development of Hurricane Ivan of 2004 between September 3rd and September 5th (see row 5 of Figure 14.3).

Raymond et al. (2011) analyzed data collected from seven aircraft missions into northwest Pacific tropical cyclone during the TPARC/TCS-08 project (THORPEX Pacific Asian Regional Campaign/Tropical Cyclone Structure experiment) in 2008. They concluded that “The formation of a strong midlevel circulation, with its associated cold core at low levels and warm core aloft, greatly aids the spin-up of a tropical cyclone by changing the vertical mass flux profile of deep convection from top heavy to bottom heavy”. We shall return to their point about the vertical profile of convective mass flux in the next subsection.

Another interesting route to tropical cyclogenesis is through mesoscale convective complexes that form over land and the drift out over warm water. Such land-based convective complexes commonly have mid-level meso-cyclones that are cold core at low levels (Bartels and Maddox 1991). A particularly interesting case of a strong mesoscale convective complex that first produced flash flooding in Pennsylvania and then formed a tropical cyclone once out over the Gulf Stream was documented by Bosart and Sanders (1981).

These observations, taken together with the route to the genesis of polar lows and medicanes described in Chapter 12, section 12.5, suggest the cold-core cyclones are suitable embryos within which to develop tropical cyclones. We will return to this subject in subsection 14.1.5.

Genesis is not always preceded by disturbances that have maximum amplitude well above the boundary layer. In the case of Gaston above, there is little evidence of a cold core in the lower troposphere, at least in the reanalysis data. (In Figure 14.5, there is evidence of a cold anomaly at 800 hPa on September 3rd, but in this case the anomaly seems to have resulted from Gaston’s circulating air mass invading the very hot Saharan air to its north.) Moreover, a careful analysis of a case of genesis in the western North Pacific by Montgomery and Smith (2012), using data from the Tropical Cyclone Structure (2008) (TCS08), showed little evidence of the an initial cold core in the lower troposphere. But, as described by Raymond et al. (2011), a mid-level vortex did develop as the system that became Typhoon Nuri reached the tropical depression stage.

Dunkerton et al.(2008) proposed that tropical cyclogenesis that is associated with tropical waves occurs within a ‘pouch’ surrounding a ‘sweet spot’ defined by the intersection of the wave axis with a critical latitude at which the phase speed of the wave equals the westward flow speed in the lower troposphere. This idea became known as the marsupial paradigm and was tested using observations made within Atlantic tropical disturbances during the Pre-Depression Investigation of Cloud Systems in the Tropics (PREDICT) experiment in 2010 (Montgomery et al. 2012; Wang et al. 2012). The basic idea is that this configuration of large-scale flow protects the inner core of nascent tropical cyclones from ventilation with low-entropy air in the lower to middle troposphere.

Early researchers, relying on sparse observations from ships and on island-based radiosondes, noted the steady progression of African easterly waves across the North Atlantic (Chapter 7, section 7.3). Dunn (1940) remarked that most of these waves crossed the North Atlantic with no development; Simpson et al. (1968) estimated that only about 10% of these waves developed during hurricane season. For some eighty years, we have observed that potential triggering disturbances are inefficient at generating tropical cyclones. At the same time, early researchers concluded that all tropical cyclones originate in pre-exiting disturbances of independent physical origin (e.g. Riehl 1948a,b; Dunn 1951; Riehl 1951; Ramage 1959; Riehl 1975) and this belief persists to this day (e.g. Vecchi et al. 2019; Sugi et al. 2020; Hsieh et al. 2020). Over the tropical Atlantic, it is clear that many tropical cyclones develop from easterly waves whose origin over Africa leaves little doubt that the formative mechanism is distinct from that of cloud clusters that form over the ocean. Historically, most observational studies have focused on the Atlantic owing to the comparatively rich observational data stream there. In the western Pacific region, in contrast, disturbances that lead to genesis originate mostly over the ocean (except in the relatively rare cases of storms that form over the eastern North Pacific or even the Atlantic and remain intact as they traverse the western Pacific). It is not entirely clear whether some of the western Pacific cyclones may form spontaneously, as happens in idealized models (section 14.2.2).

Because most of the Atlantic waves traverse the basin with little or no development, early researchers sought a third factor, beyond the presence of a tropical wave and a favorable thermodynamic and kinematic environment. Riehl (1948a,b) proposed that the third ingredient is a disturbance in the upper troposphere. Indeed, as we saw in Chapter 12, section 12.3, the quasi-balance superposition principle supports the idea that the superposition of a cyclonic disturbance in the upper troposphere with one at lower levels can increase the magnitude of surface winds, among other measures of intensity. The same physics as described in section 12.3 may operate during genesis, the only difference being the magnitude of the low-level cyclonic disturbance.

Riehl's ideas receive some support in observational studies. For example, Sadler (1967, 1976a,b) showed that transitions from tropical waves to tropical cyclones in the western North Pacific often occur when the waves approach tropical upper-tropospheric troughs (TUTTs). Hawkins and Rubsam (1968) showed that an Atlantic easterly wave developed fairly quickly into Hurricane Hilda of 1964 when it interacted with an upper tropospheric disturbance moving southeastward into the path of the wave. (Naturally, this may have been a coincidence.) The upper-level trough was remarkably small, having a half wavelength of a few hundred kilometers, and might have been missed altogether by the analysis had it not traveled through the dense radiosonde array then in place in Florida and the Caribbean. Reilly (1992) examined cases of western North Pacific cyclogenesis, using NOAA operational analyses with 2.5 degree resolution. He confined his analysis to regions rich in commercial aircraft observations and calculated the dot product of vertical shear with gradients of potential vorticity in the upper troposphere. He showed that some, but not all cases of tropical wave development were associated with anomalously high values of this quasi-balanced forcing parameter. Molinari et al. (1995) analyzed the interaction of a thin cyclonic potential vorticity filament in the upper troposphere interacting with Atlantic Hurricane Elena of 1985 and, beyond the superposition effect, emphasized the importance of the interaction of the upper tropospheric PV anomaly with the storm's anticyclonic outflow.

14.1.4: Inferences from numerical simulations

Beginning in the 1980s, a healthy interplay developed between field experiments and numerical simulations, with each approach informing the other. This subsection provides a brief synopsis of numerical experiments conducted to better understand tropical cyclogenesis.

Using a convection-permitting, nonhydrostatic, axisymmetric model, Rotunno and Emanuel (1987) showed that the RCE state of the tropical atmosphere was stable to the development of infinitesimal, tropical cyclone-like disturbances, absent interactive radiation. This was also shown to be true of a much simpler quasi-balanced axisymmetric model with parameterized convection (Emanuel 1989). But saturating the initial state of this same model, above the boundary layer, led to immediate amplification of even very weak initial vortices. It was proposed that downdrafts carrying low-entropy air into the boundary layer from the lower to middle troposphere overcame the tendency for surface enthalpy fluxes to elevate the moist entropy of the boundary layer in the nascent cyclone core. Artificially elevating the entropy of the lower and middle troposphere in the core of the initial cyclone stops this influx of low entropy to the boundary layer and allows the initial cyclone to amplify.

Partly on the basis of these findings, the Tropical EXperiment in MEXico (TEXMEX) was designed to test the hypothesis that near saturation of a mesoscale column is a prerequisite for tropical cyclogenesis. It was hypothesized that the condition of near saturation was brought about by sustained moist convection moistening a column to near saturation. However, the development of eastern North Pacific Hurricane Guillermo of 1991 proceeded from a column that had been both cooled and moistened by evaporation of rain from stratiform clouds. This column was therefore cold in the lower troposphere, and a smaller, relatively warm anomaly developed within it. The near-saturated condition appeared to have been brought about more by evaporation of rain falling from the stratiform cloud canopy than by detrainment from cumulus clouds.

Is it possible that stratiform rain from a cloud cluster could lead to genesis? To test this idea Bister (1996) inserted a “showerhead” at the center of an axisymmetric tropical cyclone model (Rotunno and Emanuel 1987) at an altitude of 4.375 km, for 36 hours, out to a radius of 116 km. (See the sketch of this configuration in Figure 14.7.) The relative humidity above the showerhead was maintained at 80% over the initial 36 hours, but no wind velocity perturbations were present in the initial condition. While the showerhead adds water mass to the system, it does not add either kinetic or moist static energy and in this respect is unique among numerical simulations of the genesis of single tropical cyclones. Water from the showerhead partially or completely evaporates as it falls, cooling and moistening the column. The sinking cool air produces inflow, maximizing in the lower to middle troposphere, and this spins up a mid-level meso-cyclone. The column under the showerhead approaches saturation by both cooling and moistening.

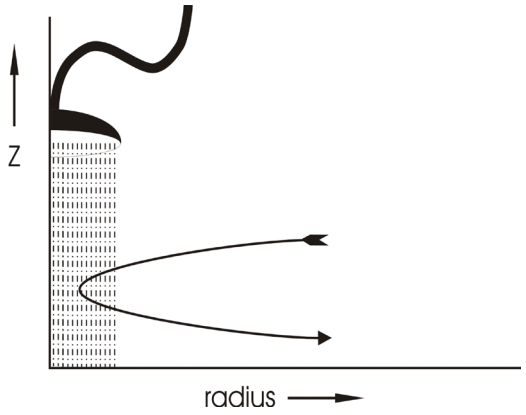

Figure 14.7: Configuration of a "showerhead" inserted into the center of the nonhydrostatic, axisymmetric model of Rotunno and Emanuel (1987). The showerhead is inserted at an altitude of 4.375 km, for 36 hours, out to a radius of 116 km, and the relative humidity is maintained at 80% in the column above the showerhead for the initial 36 hours. No kinetic or moist static energy perturbation is present in the initial state. Water from the showerhead partially or completely evaporates as it falls, cooling and moistening the column. The sinking cool air produces inflow, maximizing in the lower to middle troposphere, and this spins up a mid-level meso-cyclone. The column under the showerhead approaches saturation by both cooling and moistening.

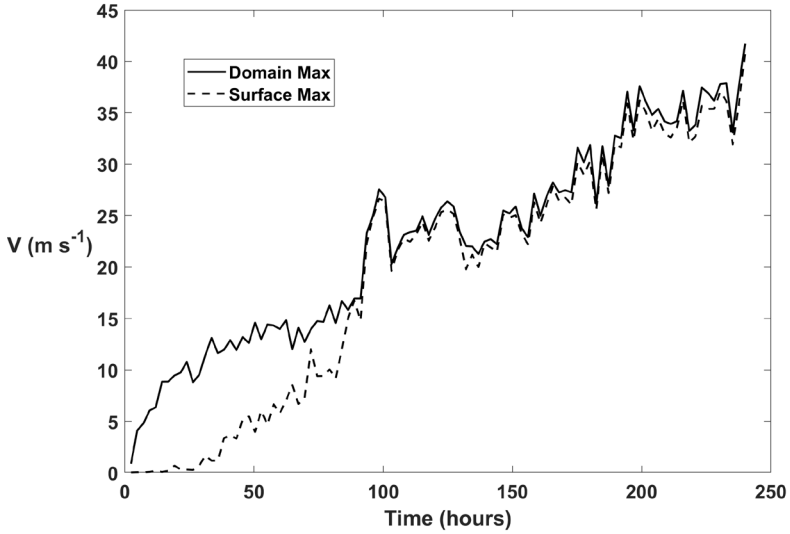

Figure 14.8: Time evolution of the domain-maximum azimuthal wind speed (m s^{-1}; solid) and maximum surface azimuthal wind speed (m s^{-1}; dashed) during a numerical simulation driven by the showerhead illustrated by in Figure 14.7.

The developments over time of the domain-maximum azimuthal wind and the maximum surface azimuthal wind are shown in Figure 14.8, for a simulation very similar to that reported by Bister (1996). The initial spin-up reflects the development of the mid-level meso-cyclone in response to the evaporative cooling. During the first 36 hours, while the meso-cyclone aloft is spinning up, there is essentially no surface wind. Over the next few days, the mesocyclone migrates downward as the condensation level lowers and the locus of maximum evaporation shifts downward. Sensible heat fluxes from the ocean cause shallow convection, which mixes angular momentum downward into the boundary layer.

At around 4 days (96 hours) into the simulation, and about 2.5 days after the showerhead has been turned off, deep convection erupts into the cold, humid core and rapid development of a deep, warm-core cyclone commences, with maximum winds at or near the surface. Figure 14.9 shows a cross-section of azimuthal velocity in a similar showerhead simulation at about the time the warm-core vortex forms inside the broader cold-core mesocyclone. This experiment suggests that given enough time, stratiform rain can lead to genesis.

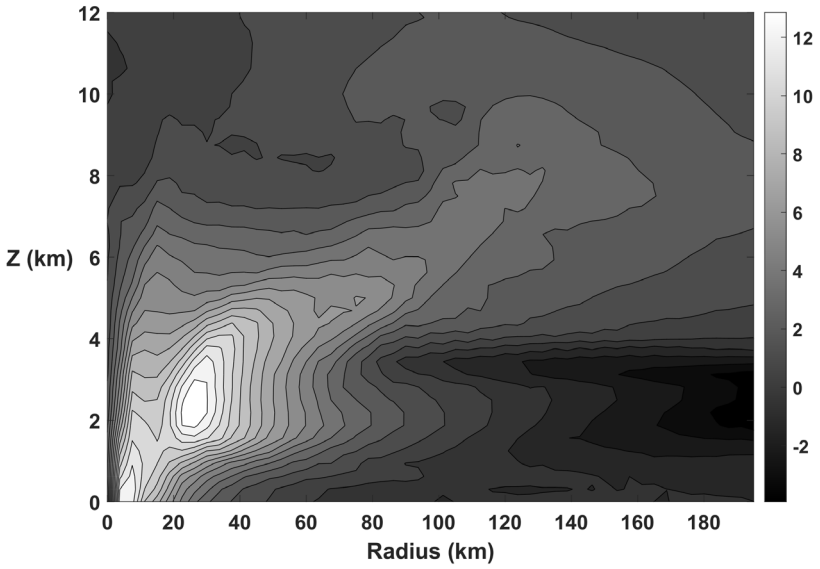

Figure 14.9: Cross-section of azimuthal wind speed (m s^{-1}) at about the time that a warm core vortex appears within the broader cold-core mesocyclone in a simulation using the non-hydrostatic, axisymmetric model of Rotunno and Emanuel (1987). This simulation was performed using a more recent version of the model, that is similar, but not identical, to that used to generate Figure 14.8.

Nolan (2007) performed fully three-dimensional simulations with the cloud-permitting Weather Research and Forecast Model (WRF) in an initial state that is ideal for tropical cyclone formation, with high sea surface temperature and a deep, convectively adjusted troposphere with no mean wind at any level. The model was initialized with a weak, warm-core vortex. Despite these ideal conditions, the initial surface vortex decayed and rapid development did not occur until 48-60 hours after initialization. During this gestation period, the troposphere gradually moistened from both detrainment and evaporation of precipitation from cumulonimbi. When the relative humidity in the core exceeded about 80%, systematic inflow ramped up at mid-levels and a mesoscale cyclone developed at those levels. As it intensified and the core humidity approached saturation, a smaller-scale, warm-core vortex developed within the larger-scale mesocyclone and intensified rapidly while evolving toward a classical mature tropical cyclone.

A somewhat similar study was conducted by Davis (2015) using a different model, but rather than initializing with a weak warm core vortex, he simulated radiative-convective equilibrium (on an *f*-plane, as in Nolan's study) starting from extremely small random perturbations. As in other studies of self-aggregating convection in rotating domains (see Chapter 3, section 3.4), convection slowly aggregated into non-rotating clumps after about 10 days, and these begin to exhibit rotation after around 20 days. These rotating clusters gradually merge into a single

system with a prominent mid-level vortex and a cold core in the lower troposphere. From this point on, the development is like that described by Nolan (2007), with relative humidity increasing at all levels, and a smaller scale, warm-core vortex developing very rapidly within the larger, cold-core mesocyclone. Once the mid-level mesocyclone forms, which takes more than 50 days from the initial state, the whole development proceeds at fast time scales of a few days consistent with those found by Nolan (2007) and Bister (1996). Davis (2015) emphasizes the importance of downdrafts that occur during the formation and development of the mesocyclone. These bring low entropy air from the lower and middle troposphere in contact with the warm sea surface, enhancing the surface enthalpy flux and thereby increasing the column-integrated moist static energy. They way also help to transport momentum from the mid-level cyclone down into the boundary layer, giving an impetus to the subsequent development of the warm-core vortex.

Using the WRF model, Nolan et al. (2007) explored the sensitivity of genesis to parameters and initial conditions, starting from radiative-convective equilibrium states on an *f*-plane with no mean wind. While spontaneous genesis occurred in as few as 15 days, the process was greatly accelerated by placing a weak vortex in the initial condition. While this vortex had peak amplitude at mid-levels, and was therefore cold core in the lower troposphere, it did extend down to the surface. The time to genesis, (defined as the first time the rate of central surface pressure fall exceeded 25% of its maximum value during the rapid intensification phase) decreased as the amplitude of the initial mesocyclone increased. They also showed that the time to genesis decreases with increasing potential intensity. This work, together with subsequent research, shows that while spontaneous genesis is theoretically possible in ideal environments, it takes tens of days, whereas even weak “triggering” disturbances can greatly accelerate the process, particularly if they have low-level cold cores that are nearly saturated.

Nolan and Rappin (2008) and Rappin et al. (2010) extended the work of Nolan et al. (2007) by including wind shear in the RCE state. As found in observational studies and other numerical work, wind shear impedes and may prevent genesis. Rappin et al. (2010) introduced a nondimensional “incubation parameter” (identical to Tang and Emanuel’s (2010) “ventilation parameter”) defined

$$\Lambda \equiv \frac{V_s}{V_p}\frac{h_b - h_m}{h_0^* - h_b}, \tag{14.1}$$

to quantify the effect of vertical wind shear on genesis. (See also equation (12.23) in Chapter 12.) Here, V_s is the magnitude of the imposed wind shear, V_p is the potential intensity, h_b is the environmental boundary layer moist static energy, h_m is a representative measure of the environmental moist static energy in the lower to middle troposphere, and h_0^* is the saturation moist static energy of the sea surface. They found that the time to genesis from a 10 m s^{-1} mid-level mesocyclone is highly correlated with this incubation parameter. (For a particular choice of the definition of time to genesis, the correlation coefficient is 0.94.). The greater the incubation parameter, the longer the time to genesis. Note, however, that Nolan et al. (2010) only considered a single magnitude of wind shear (5 m s^{-1} between 850 and 200 hPa), but Nolan and Rappin (2008) had explored the effects of a range of wind shear magnitudes. As shown in the theory developed by Tang and Emanuel (2010), there is a critical value of Λ beyond which intensification is impossible. Nolan et al. (2010) varied Λ by changing the imposed sea surface

temperature. At higher temperatures, both V_p and $h_0^* - h_b$ are larger, but this is overwhelmed by the increase in the subsaturation of the lower to middle troposphere as represented by $h_b - h_m$ in (14.1). Therefore, in RCE, increasing sea surface temperature holding wind shear constant should decrease the rate of cyclogenesis, if the statistics of triggering disturbances remain constant. We shall return to this issue in Chapter 15.

Dry air above the boundary layer has a strong influence on the effect of shear, as reflected in the incubation or ventilation parameter given by (14.1). But even in the absence of shear, the degree of sub-saturation and proximity of dry air to the nascent storm core has a strong influence on its development (Braun et al. 2012; Nolan and McGauley 2012). The storm core must become nearly saturated before strong development can occur, and this takes more time to accomplish if there is initially more dry air in or near the core.

While shear is almost always an obstacle to storm intensification, Nolan and McGauley (2012), using the WRF model, showed that moderate shear can hasten the formation of low-level vortices, at least given an initial mid-level vortex, but such vortices generally did not develop much after formation. This is also consistent with the observational study by Molinari et al. (2004). They analyzed the formation of Hurricane Danny of 1997 and showed that shear caused a sequence of cluster and mesovortex developments, the last of which finally developed into a tropical cyclone when the environmental shear had relaxed. They concluded that the shear assisted the earlier, sequential development.

These and other numerical simulations, combined with observationally based studies, lead to a conceptual view of how individual tropical cyclones develop, given a favorable environment. This is presented in the next subsection.

14.1.5: Synopsis of the local view of tropical cyclogenesis

Post-war researchers rapidly came to the view that tropical cyclogenesis does not take place spontaneously but needs to be triggered. As Riehl (1948a) put it, “In the cases of hurricane formation noted in the course of the study, deepening began, without exception, in pre-existing perturbations”. Riehl and Kleinschmidt understood that mature tropical cyclones are powered by enthalpy fluxes from the sea, but also suspected that other factors are at work in their genesis. They knew that only a small fraction of cloud clusters during hurricane season end up becoming tropical cyclones. Riehl, in particular, thought that the transformation of a wave disturbance into a tropical cyclone was cause by interactions with upper tropospheric disturbances (Riehl 1948b) and differential radiative cooling caused by the dense cirrus canopy of cloud clusters (Riehl 1963).

It is notable that European researchers had rejected the idea that genesis is powered by latent heat stored in the atmosphere, a hypothesis dating back to the work of Espy (1841). Already, von Hann (1901) had reasoned that ‘‘that since a thundercloud does not give any appreciable pressure-fall but generally even a pressure-rise, it would be unreasonable to assume that a magnifying of this process would cause the strongest pressure falls known’’ (quoted in Bergeron, 1954). Riehl, noting that “many of the heaviest tropical rainfalls occur without the existence of a cyclonic circulation, and even closed depressions with torrential precipitation often fail to deepen” calculated that releasing all the CAPE stored in the tropical atmosphere,

generously using surface-based lifting along a pseudo-adiabat, would lower the surface pressure only to about 1,000 hPa (Riehl 1954). He later remarked that “it has never been easy to see how such an increment [referring to observed pressure falls] can be obtained from internal storm characteristics only” (Riehl 1975). Nevertheless, many textbooks still claim that tropical cyclones are powered by latent heat release, and various forms of this idea continue to appear in the literature in connection with genesis (e.g. Ooyama 1964; Charney and Eliassen 1964; Montgomery and Enagonio 1998; Montgomery et al. 2006; Kilroy et al. 2017). Given the often magnificent appearance of cumulonimbi, the idea that deep moist convection drives genesis is understandable but undermined by the discovery that tropical cyclones can form in dry-adiabatic atmospheres with no moist convection (Mrowiec et al. 2011; Cronin and Chavas 2019; Velez-Pardo and Cronin 2023).

On the contrary, a strong case can be made that moisture in the atmosphere impedes genesis even though it permits ultimately stronger vortices given constant potential intensity (Cronin and Chavas 2019). In dry adiabatic atmospheres in RCE, there is no strong entropy minimum in the middle troposphere as we find in the moist case. Consequently, there is no reservoir of low entropy air to enter the boundary layer during genesis and prevent the boundary layer entropy from increasing. Experiments with a dry version of a nonhydrostatic axisymmetric model show that very small amplitude initial vortices amplify (Figure 14.10).

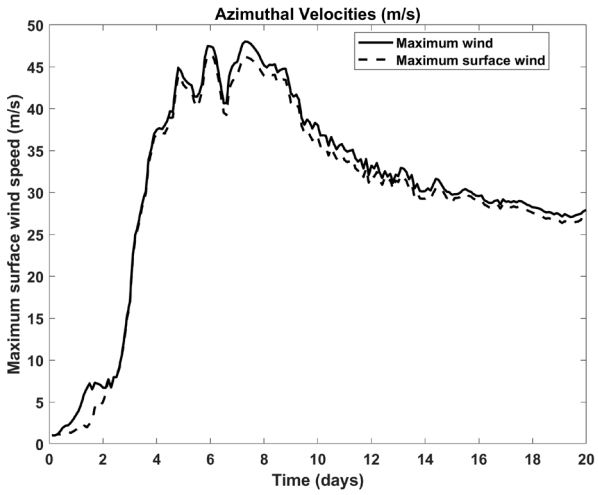

Figure 14.10: Domain-maximum (solid) and surface-maximum (dashed) azimuthal velocities in a dry version of the nonhydrostatic axisymmetric model of Rotunno and Emanuel (1987) with no damping of temperature perturbations. Initial warm-core vortex amplitude is about 1 m s^{-1}.

Note that in a dry RCE state, the ventilation (or incubation) parameter given by (14.1) vanishes because $h_b - h_m$ is nearly zero. Also, as noted before, as temperature increases in the moist RCE state, the ventilation parameter generally increases (depending to some extent on what forces the temperature increase), thereby increasing the main inhibition to genesis. Moisture makes genesis harder. (At the same time, other processes, like cloud-radiation feedbacks, that tend to enhance genesis may also increase with temperature.)

Through all the observational and numerical model studies reviewed in the previous section, with all the different particular routes to genesis, there is a common thread: Whatever happens, a mesoscale column of the atmosphere must become nearly water saturated before real

development can take place. Given that the density temperature lapse rates are seldom steeper than a reversible moist adiabat, this near saturated condition is equivalent to a state in which the moist static energy does not change much with altitude. (This is always true in dry RCE states since the static energy is constant with height in such states; there is no inhibition to overcome.)

The need for near saturation is consistent with the finding that in standard moist convection in an unsaturated environment, almost all of the irreversible entropy production is used up in mixing across water vapor gradients and by frictional dissipation of falling rain, with very little left over for kinetic energy dissipation (Pauluis and Held 2002). The environment must approach quite close to saturation before the system transitions to one in which dissipation of wind energy is the dominant irreversible process.

There are three ways to make the moist static energy constant with height starting from a typical tropical state (or a moist RCE state), as illustrated with the aid of Figure 14.11.

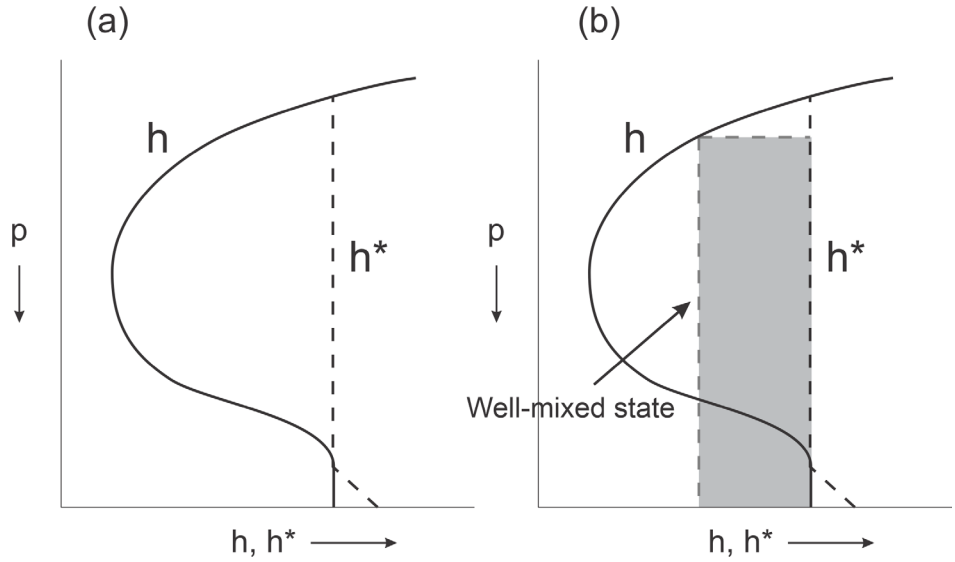

Figure 14.11: a) Typical profiles of moist static energy, h, and saturation moist static energy, h, in the tropical atmosphere. b) Same as a) but showing an additional profile (vertical dashed line in middle of plot) that represents both h and h* of a state that results from conservative vertical mixing of moist static energy. The difference between the initial and final profiles of h* is shaded in gray.*

There are three (not mutually exclusive) ways to create a saturated, vertically uniform distribution of moist static energy:

1. Add enough moist static energy to the column to bring it to saturation. This would entail filling in the whole area between the h and $h*$ curves in Figure 14.11a.

2. Mix the column vertically to homogenize the moist static energy without adding or subtracting column-integrated moist static energy. This state is indicated by the dashed vertical line in the center of Figure 14.11b. Note that the resulting column, having a smaller $h*$ than the initial state, will therefore be colder.

3. Lift the whole column over an extended time. Given a positive value of the gross moist stability, this will require work to be done on the column by some external disturbance. The final moist static energy profile may somewhat resemble the profile that results from mixing.

In the first case, large quantities of energy would have to be added to the column. For a randomly chose tropical sounding (the island of Koror in the western tropical North Pacific at 12 GMT on 1 April 2018), about $3.6 \times 10^8 \, J \, m^{-2}$ would have to be added to the column to bring it to saturation without changing its temperature. A surface enthalpy flux of $150 \, W \, m^{-2}$ would have to be sustained over about 28 days to achieve this, with complete blockage of outgoing longwave radiation by high clouds. This is about the time scale for spontaneous aggregation of moist convection through cloud-radiation interactions (Davis 2015; Wing et al. 2016). Very few tropical cloud clusters stay over warm water this long, so is unlikely that process 1) can lead to genesis by itself in the real world, though to be sure, cloud-radiation interactions contribute tangibly to genesis (Riehl 1963; Muller and Romps 2018).

Process 2) in its pure form does not change the column-integrated moist static energy (by design) and leads to a state that is water saturated but somewhat colder than the initial state. This state cannot exist on time scales longer than those associated with internal gravity waves unless the column is rotating and in thermal wind balance. It is important to note that cooling and moistening by evaporation of rain, accompanied by moist adiabatic adjustment, can also accomplish this. The operation of process 2) and/or 3) is consistent with the observation and modeling result that developing cloud clusters usually pass through a cold-core state with cyclonic vorticity at mid-levels. The process of bringing a column to saturation by process 2) or 3) can be substantially faster than by route (1). There is no need for a mid-level cyclonic disturbance to be present from the beginning; it should be regarded as something that occurs along the road to genesis.

The development of a tropical cyclone might be thought of as occurring in four stages, as illustrated in Figure 14.12.

In the first stage, a cloud cluster is triggered by some external disturbance such as a tropical wave or an extratropical front or upper tropospheric disturbance moving into the tropics. There are apparently many ways this can happen. The cloud cluster has a high, dense cirrus canopy with low effective infrared temperatures. Downdrafts import low entropy air from the lower and middle troposphere into the boundary layer. This stage can and often does take place over land.

During the second stage, much of the original deep convection diminishes and may even disappear, but the high cloud canopy remains largely intact. Evaporation of rain and mixing by shallow cumuli and congestus clouds cool and moisten the lower troposphere, and inflow at mid-levels gradually spins up a mesocyclone in the middle troposphere. This mesocyclone may slowly migrate downward, and shallow convection may transfer some angular momentum into the boundary layer. Any lowered boundary layer moist static energy begins to recover. The dense cirrus canopy blocks outgoing longwave cooling, allowing surface fluxes to gradually increase the column moist static energy. This gestation period can be disrupted or terminated by wind shear and/or passage over land or cold water; otherwise, it usually lasts a few days.

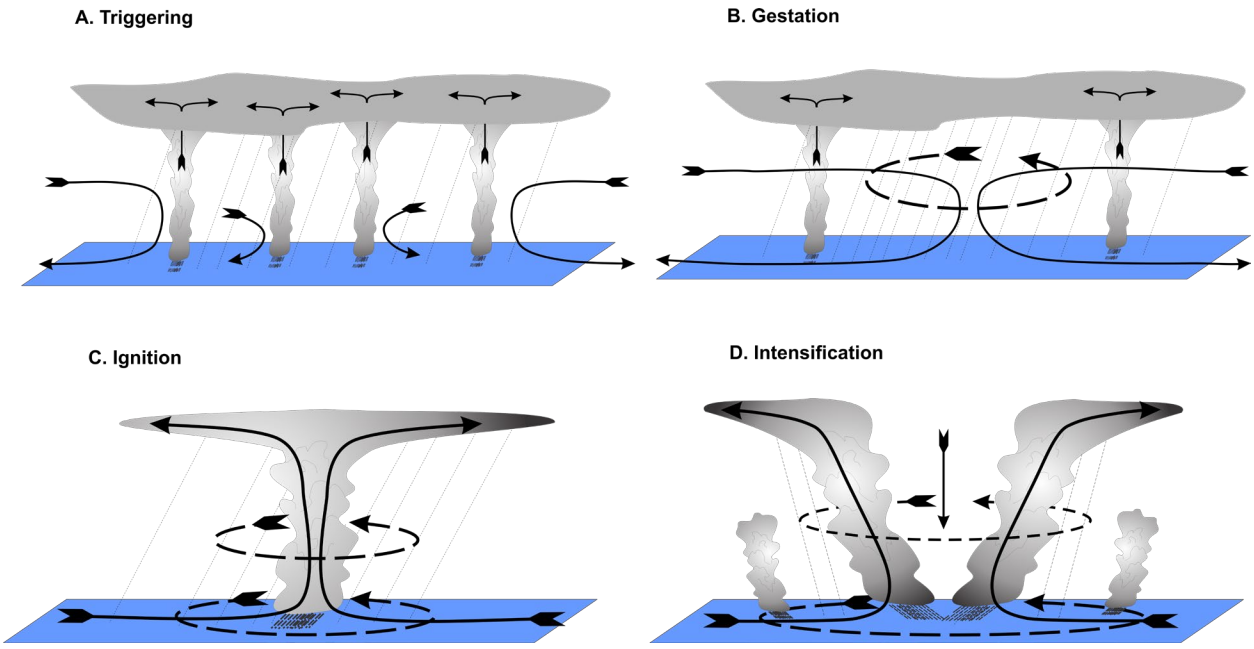

Figure 14.12: Four stages in the development of a tropical cyclone. A.) Triggering: A cloud cluster is initiated by one or more of a set of possible processes; b) Gestation: While the deep convection may diminish, the stratiform rain area persists and mid-level inflow continues, driven by evaporation of rain and melting of snow. The air cools and moistens, and the inflow gradually spins up a mid-level mesocyclone. This stage typically lasts a few days. C) Ignition: A new episode of deep convection penetrates the pre-moistened, cool air in the center of the mesocyclone. Downdrafts are weak and their moist entropy is not greatly depressed. Inflow and cyclonic spin up commence in the boundary layer. D) The WISHE feedback between intensifying surface winds and surface enthalpy fluxes leads to an intensifying tropical cyclone

When the air near the center of the mid-level mesocyclone becomes humid enough, and the boundary layer moist static energy has increased sufficiently, a new episode of deep convection erupts. Because the troposphere in the core of the system is nearly saturated, the deep convection can produce only weak downdrafts, though stronger downdrafts may occur outside the core. Inflow into the deep convection occurs in the boundary layer, and cyclonic vorticity develops rapidly there. In this ignition stage, the feedback between wind and surface enthalpy flux becomes active and the system begins to intensify as a tropical cyclone, leading to the final (and sometimes rapid) intensification phase.

This paradigm fits much of the field experimental observations and numerical modeling results presented in the previous subsections. On the basis of his analysis of satellite imagery, conventional observations, and airborne reconnaissance data collected in the early 1980s, Zehr (1992) developed a paradigm similar to the one described in Figure 14.12. He begins by stating that “Tropical cyclogenesis in the western North Pacific is typically characterized by an early convective maximum which precedes the initial appearance of a tropical depression” and suggests that this early maximum is a result of synoptic-scale forcing. He then states that “A weak mesoscale vortex is initiated which is located within the larger broad-scale cyclonic circulation of a pre-existing tropical disturbance…..This early convective maximum and associated mesoscale vortex formation precede first designation as a tropical storm by an average period of about 3 days.” Zehr includes our stage 2 as part of his first stage: “Stage 1 also includes the period following the convective maximum where the overall convection is considerably reduced. It is typically during this period that a distinct low-level circulation center can first be identified, and persistent cyclonically curved convective cloud lines are observed.”

Zehr's second stage is equivalent to our third: "The end of Stage 1 and the onset of Stage 2 is marked by the onset of increasing deep convective activity associated with a low-level circulation center. It is usually during Stage 2 that the disturbance is first designated as a tropical depression."

Based on their analysis of five tropical disturbances that formed in the northwest Pacific region in August and September of 2008, during the TPARC/TCS-08 project, Raymond et al. (2011) conclude that "The formation of a strong midlevel circulation, with its associated cold core at low levels and warm core aloft, greatly aids the spin-up of a tropical cyclone by changing the vertical mass flux profile of deep convection from top heavy to bottom heavy." They go on to remark that "This has two effects: (1) the enhancement at low levels of the convergence of mass and hence vorticity, thus aiding the spin-up of a warm-core vortex and (2) the suppression of the lateral export of moist entropy by deep convective inflows and outflows from the core of the developing system." The bottom-heavy upward mass flux by convection is also consistent with the absence or near absence of strong evaporatively driven downdrafts, enabling strong convergence and spin-up at low levels. This also has the effect of tamping down the inward flux of low entropy air at middle levels that characterizes the second stage of development in our paradigm.

The spin up at middle levels during stage 2 need not be initially concentrated in a single mesocyclone but may be distributed among a number of smaller mesocyclones which eventually merge into one (e.g. Davis 2015).

Raymond et al. (2011), along with Dunkerton et al. (2008), Wang et al. (2010), Montgomery and Smith (2012), and Montgomery et al. (2012) emphasize the vulnerability of stage 2 (in our nomenclature) to external disruption. They suggested that external flow configurations that are favorable to closed trajectories of air parcels in the lower to middle troposphere, relative to the translating cloud cluster, are necessary to avoid intrusions of low entropy air into the cores of developing disturbances. As the mesocyclone at mid-levels intensifies, its inertial stability also acts as a break on dry air intrusion.

Stage 2 can be skipped altogether with strong enough synoptic-scale forcing. For example, in the case of medicanes and polar lows, the large-scale trigger is itself a cold-core system with a humid interior, providing the favorable embryo in which a warm core tropical cyclone-like disturbance may amplify. The genesis of Atlantic Hurricane Diana of 1984 occurred as an intense cyclonic potential vorticity anomaly at the tropopause broke off from its parent Rossby wave. The formation of an intense, cold, saturated core through strong ascent in response to this development, together with the quasi-balanced forcing of cyclonic vorticity at the surface, both triggered and "ignited" the development of Diana (Bosart and Bartlo 1991).

This concludes our summary of some of the extant thinking on the local view of tropical cyclogenesis. We next turn to a global view of genesis.

14.2 The global view

The global view of tropical cyclogenesis inquires about the environmental factors that govern the statistics of genesis, including its global frequency, spatial and seasonal variations, and response to natural and anthropogenically forced variability. In a more advanced form, it could account for feedbacks of tropical cyclones on the climate system; a discussion of this idea will be deferred to Chapter 15.

14.2.1 Genesis indices

One approach to understanding the physical basis of the observed climatology of tropical cyclones is to see how it is correlated with known physical properties of the climate system. Palmén (1948) was probably the first to address the physical basis of the observed climatology of tropical cyclones. He believed that such storms are powered by CAPE stored in the tropical atmosphere and showed that they only occur over those portions of the oceans where CAPE is usually positive. He demonstrated that this condition is strongly correlated with region in which the sea surface temperature exceeds 26-27°C. Palmén also recognized that tropical cyclones do not develop where the magnitude of the Coriolis parameter is too small.

Gray (1975, 1979) developed the first genuine genesis index and tested it against observed spatial and seasonal variations of tropical cyclone activity. Gray's "seasonal genesis parameter" was defined (with some changes of notation) in terms of seasonal mean variables:

$$SGP = C \underbrace{f \frac{\zeta \pm 5\times10^{-6} s^{-1}}{|\Delta \mathbf{V}| + 3 m s^{-1}}}_{Dynamic} \underbrace{K_o \left(\theta_{eb} - \theta_{em} + 5K\right)\left(\mathcal{H} - 40\%\right)}_{Thermodynamic}, \tag{14.2}$$

where C is a (dimensional) constant, f is the Coriolis parameter, ζ is the low-level relative vorticity (in units of s^{-1}), $|\Delta \mathbf{V}|$ is the magnitude of the vector wind shear between 950 hPa and 200 hPa (in $m s^{-1}$), θ_{eb} and θ_{em} are the equivalent potential temperatures (in K) in the boundary layer and at 500 hPa, respectively, $\mathcal{H}$ is the relative humidity (in %) in the middle troposphere, and the "ocean thermal energy", K_o, is defined as

$$K_o \equiv \int_0^{60\,m} \rho_w c_w \left(T - 26\ ^oC\right) dz, \tag{14.3}$$

where ρ_w is the density of seawater, c_w is its heat capacity, and T is the seawater temperature in ^oC. The integrand in (14.3) is bounded below by zero, and the relative humidity in (14.2) is bounded below by zero and above by 100%. In the third factor in (14.2), the plus sign I used in the northern hemisphere, and the minus sign in the southern.

Gray emphasized that favorable conditions for genesis can be thought of as consisting of thermodynamic contributions and dynamic (or kinematic) contributions.

The index recognizes that tropical cyclones do not form very near the equator, where the Coriolis parameter vanishes, and may be more likely to form where the seasonal mean vorticity is already large, such as in a poleward-displaced ITCZ. His deep tropospheric shear factor appears in the denominator since shear is usually detrimental to genesis. It was also recognized

that a dry lower to middle troposphere is not conducive to genesis. But two of his factors have less physical justification. Gray, like Palmén and some researchers of that era, thought that the degree of conditional instability is important, and mistakenly equated that with the negative vertical gradient of moist entropy in the lower troposphere. Subsequent observational and model-based studies clearly show that genesis is inversely proportional to this gradient. But Gray's mid-tropospheric relative humidity factor works in the oppositive direction and it can be shown that the product of the two factors is nearly constant. This leaves only K_o as an important thermodynamic predictor.

But there are two problems with K_o. First, it has an arbitrary threshold sea surface temperature of 26°C, and while that worked reasonably well in the climate of that era, it is now understood that a threshold, even if it is justified, changes with climate. Second, although upwelling of cold water is an important influence on mature tropical cyclones, as we discussed in Chapter 13, there is little evidence that the temperature of water much below the surface has any effect on genesis.

Inspired by the success of Gray's seasonal genesis parameter, other genesis indices were developed more recently (Emanuel and Nolan 2004; Emanuel 2010; Tippett et al. 2011; Bruyère et al. 2012). Based on both theory and models, potential intensity was substituted for sea surface temperature and shear and vorticity factors were retained, although the latter appears to enter as more of a threshold effect (Tippett et al. 2011). Nondimensional numerical models (e.g. Emanuel 1989, 1995) point to the saturation deficit of the middle troposphere being the relevant humidity factor, rather than relative humidity (Emanuel 2010). Rappin et al. (2010) and Tang and Emanuel (2010) proposed that the humidity, shear, and potential intensity factors should enter as a particular nondimensional ratio of the shear and the potential intensity, all multiplied by a nondimensional measure of the saturation deficit of the middle troposphere. This nondimensional ratio was shown by Rappin et al. (2010) to be highly correlated with the length of time for a weak initial vortex to begin to amplify at a substantial rate. Genesis indices have been found to correlate with modulation of tropical cyclones by El Niño–Southern Oscillation (ENSO; Camargo et al. 2007a) and the Madden Julian oscillation (MJO; Camargo et al. 2009), and to account for some aspects of climate change simulated by climate models (Camargo et al. 2007b; Zhang et al. 2010; Korty et al. 2012a,b; Camargo 2013; Emanuel 2013, 2020).

The "genesis potential index" (GPI) developed by the author (Emanuel, 2010) was constrained to be dimensionally consistent, yielding a genesis rate in terms of number of cyclones per unit area per unit time. That index is

$$GPI \equiv C \frac{|\eta|^3 \, \chi^{-4/3} \left(V_{pot} - 35 ms^{-1} \right)^2}{(25 ms^{-1} + S)^4}, \tag{14.4}$$

where C is a dimensionless constant, η is the absolute vorticity, V_{pot} is the potential intensity (in ms^{-1}), S is the magnitude of the 250 hPa to 850 hPa wind shear (in ms^{-1}), and χ is a nondimensional measure of the subsaturation of the lower to middle troposphere:

$$\chi \equiv \frac{s^* - s_{600}}{s_0^* - s^*}, \tag{14.5}$$

where $s*$ is the saturation entropy of the troposphere (which is nearly constant with height in a moist adiabatic atmosphere but which is in practice evaluated at 600 hPa), s_{600} is the actual moist entropy at 600 hPa, and s_0^* is the moist entropy of air saturated at sea surface temperature and pressure. The factor $\left(V_{pot} - 35 ms^{-1}\right)^2$ is set to zero for all potential intensities less than $35 ms^{-1}$. The predictors in (14.4) were chosen to match the inputs to a simple, nondimensional numerical model (Emanuel 1995) and the various coefficients were chose to optimize the index's ability to predict spatial and temporal variability of observed genesis.

The exponents and numerical factors in (14.4) were optimized using monthly-mean values of the variables from reanalysis data. The GPI is designed to be used with monthly-mean inputs.

This and other *GPI*s are modestly successful at capturing the spatial distribution of genesis. Figure 14.13 compares the *GPI* given by (14.4) and applied to European Center CERA-20C monthly mean[1] reanalysis data (Laloyaux et al. 2018), summed over the period 1980-2010, with genesis points during the same period from standard IBTrACS historical data (Knapp et al. 2010).

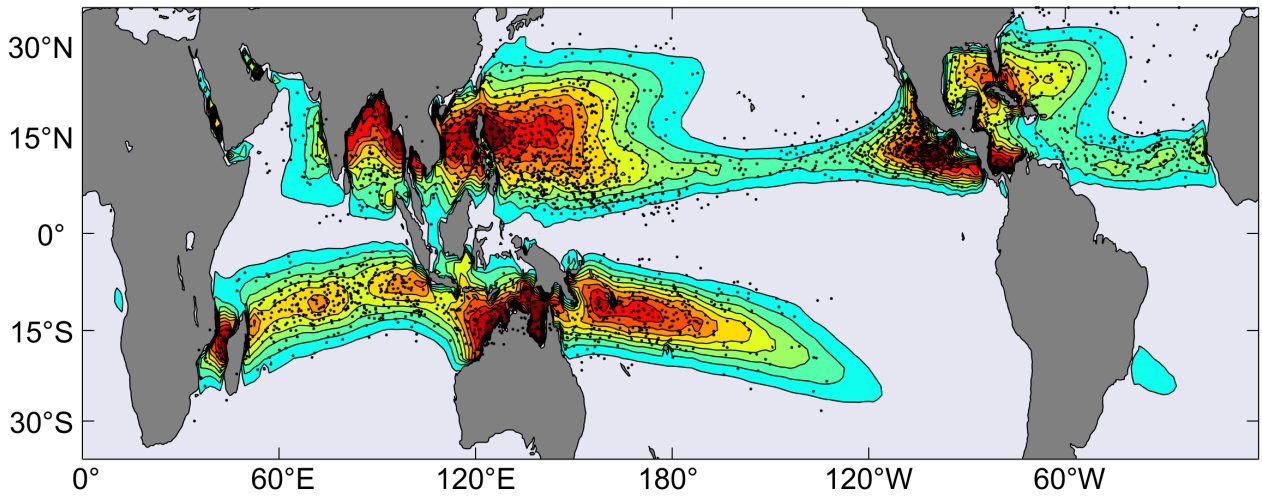

Figure 14.13: Genesis Potential Index given by (14.4) summed over the all the months from January, 1980 through December, 2010 (contours) from CERA-20C reanalyses, and first track points (black dots) in the IBTrACS historical data over the same period.

For the most part, there is a reasonable correspondence between the index and the density of genesis points. The index misses some subtropical developments, especially in the North Atlantic. This is likely owing to tropical transitions and to developments that take place under cold-core, cutoff cyclones aloft, in which the air is anomalously close to saturation and the potential intensity is elevated over its monthly mean values. Here the *GPI* based on monthly mean inputs may be somewhat smaller than the monthly mean of *GPI*s calculated with daily values. Also, in the central Pacific region as well as the North Indian Ocean, there are several

[1] For the shear in (14.4), shear magnitudes were calculated each day and then averaged over each month. For all other inputs to (14.4), monthly mean quantities were used.

instances of genesis equatorward of expectations based on the *GPI*. These are places where the daily values of relative vorticity may occasionally be somewhat larger than the monthly mean values, so here again the *GPI* based on monthly mean inputs may be smaller than that based on daily data and then averaged over a month.

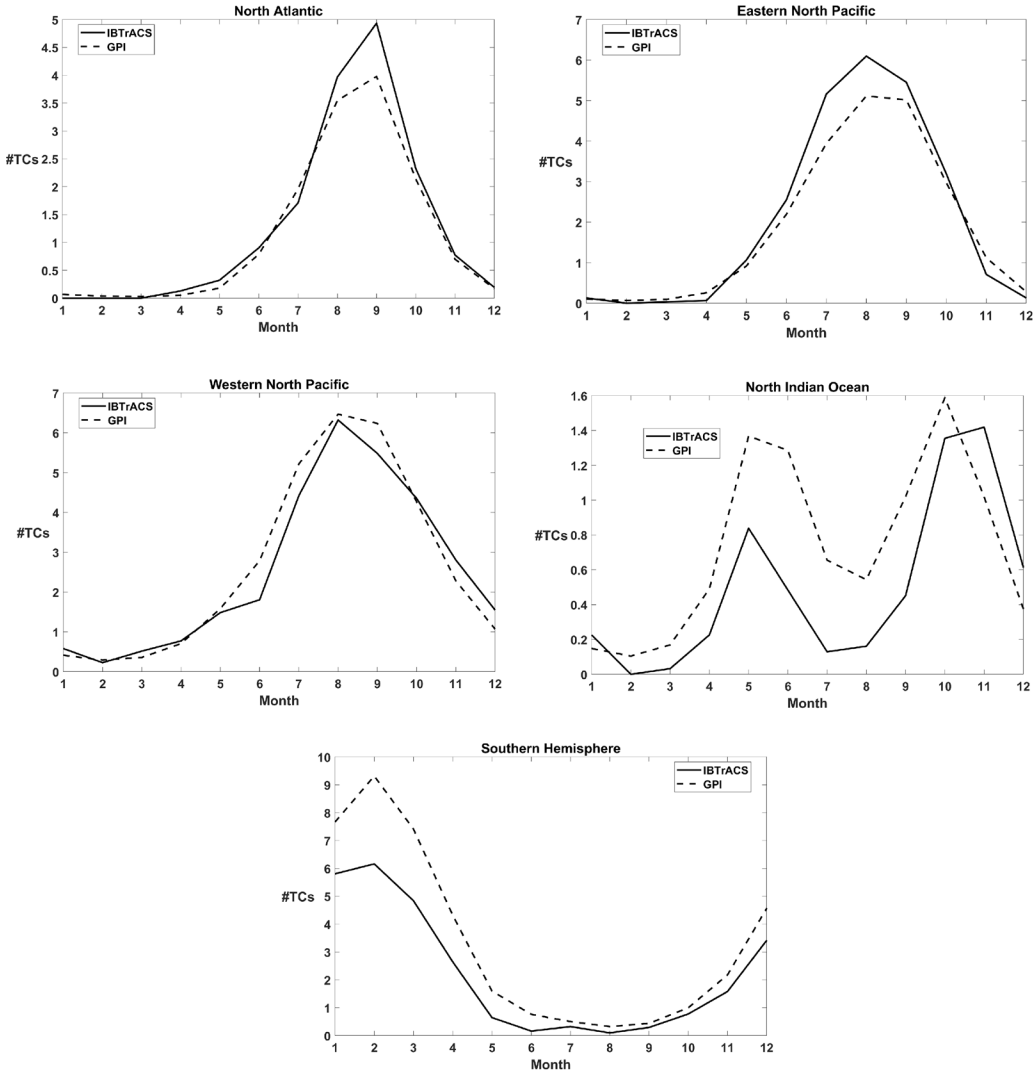

Figure 14.14: Monthly frequency of tropical cyclones in five ocean basins, from IBTrACS data (solid) and from the genesis potential index (GPI) given by (14.4) and applied to CERA-20C reanalyses (dashed). Both frequencies have been averaged over the period 1980-2010.

The seasonal cycle of the *GPI* given by (14.4) is compared to historical data in Figure 14.14. The index captures the seasonal cycle quite well, but over-predicts activity in the North Indian Ocean and in the southern hemisphere, and underpredicts overall activity in the North Atlantic and eastern North Pacific basins.

Comparison of the annually summed *GPI* given by (14.4), driven by CERA-20C reanalyses, with annual tropical cyclone frequencies in the North Atlantic region from 1980 to 2014 yields a correlation coefficient of about 0.75, so that more than half of the interannual variations in cyclone counts are “explained” by the *GPI*. Since roughly half the observed variance is consistent with a pure Poisson random process, the *GPI* accounts for most or all the rest. But

interannual variations of the *GPI* do not explain the observed interannual variability in other ocean basins, and by construction, *GPI* cannot explain the global mean count of about 90 storms per year, given the presence of the dimensionless constant C in (14.4), that must be tuned to give the correct annual global mean.

In summary, *GPI*s, which are based strictly on large-scale, time mean (usually monthly mean) variables, predict much of the spatial, and seasonal variability of tropical cyclones, and their response to large-scale phenomena such as ENSO and the MJO. They also predict much of the non-random interannual variability of tropical cyclones in the North Atlantic. The underprediction of genesis activity in the North Atlantic and eastern North Pacific may point to a role for triggering disturbances, like African easterly waves, in those places. Likewise, the overprediction of cyclones in the southern hemisphere may be owing to a dearth of triggering disturbances there. Finally, the over-prediction of genesis in the North Indian Ocean may simply be owing to there not being enough space for tropical cyclones to develop in the confines of the Bay of Bengal and the Arabian Sea.

Yet observations show that most if not all tropical cyclones originate in pre-existing disturbances. These disturbances are largely if not entirely filtered out in taking monthly means, so we are left with the seeming paradox that while cyclones originate in pre-existing disturbances, the climatology of those disturbances does not appear to play a large role in the climatology of tropical cyclones.

A strong clue to the resolution of this paradox is provided in the work of Patricola et al. (2018) and Danso et al. (2022). They examined tropical cyclone formation during the North Atlantic seasons of 2005 and 2020, respectively, using a regional, convection-permitting model (WRF; Skamarock et al. 2019) covering the tropical North Atlantic and driven by time-evolving sea surface temperatures and lateral boundary conditions supplied by the European Center for Medium-Range Weather Forecasts (ECMWF) ReAnalysis (ERA5; Hersbach et al. 2020). They ran a ten-member ensemble for the 2005 season and a three-member ensemble for the 2020 season, with ensemble members differing only in their initial conditions.

In each case, and for each ensemble member, they ran a control experiment with full, time-dependent boundary conditions and a second set in which a filter was applied at the eastern boundary of the domain, near the African coast, that filtered out all variability in the range of 2-10 days. This range includes African easterly waves (AEWs). They found that as many or more tropical cyclones formed when AEWs were suppressed, but under suppressed conditions storms tend to form further west and become more intense, perhaps because more of the tracks moved into the western Atlantic and Gulf of Mexico, where potential intensities are usually higher. Moreover, in the control experiment, the locations and timings of genesis were highly correlated among ensemble members and with measures of AEW location and time, while in the experiments with AEWs suppressed, the locations and timings of genesis were uncorrelated among ensemble members.

It would seem from these experiments that while potential initiating disturbances like AEWs indeed determine *when* and *where* tropical cyclones form, they may not determine *if* they form.

It should be recognized, however, that although 2-10 day variability was filtered from the eastern boundary and succeeded in suppressing AEWs, disturbances outside that frequency range could still pass through the eastern boundary, and variability at all sub-seasonal frequencies

could develop within the domain or enter through the northern and southern boundaries. But the lack of correlation of genesis location and timing among ensemble members with 2-10-day variability suppressed at the eastern boundary makes it unlikely that TCs were being triggered by any disturbances entering through the boundaries.

This view of genesis climatology suggests that genesis is more “fuel-limited” than “trigger-limited”.

It should also be recognized that there is appreciable interannual variability of AEW activity and those variations may be weakly correlated with Atlantic tropical cyclone metrics (Thorncroft and Hodges 2001). While such a correlation may point to a causal relationship between AEWs and genesis, it is also possible that larger-scale conditions affect both phenomena in the same direction.

Finally, at the opening of this chapter, we remarked that the observed global number of tropical cyclones is around 90, with a variance around that number consistent with pure Poisson variability. When we calculate that number from globally summed monthly GPI (14.4) applied to the CERA-20C reanalysis over the whole period 1901-201, we see a time series with no trend and with a variance about the mean of only about 38% of what would be expected from a pure Poisson process (Figure 14.15). This suggests that much of the observed global variability is related to randomness associated with triggering and/or sub-monthly variability of the large-scale environment.

We next turn to a description of tropical cyclone climatology in idealized climate states.

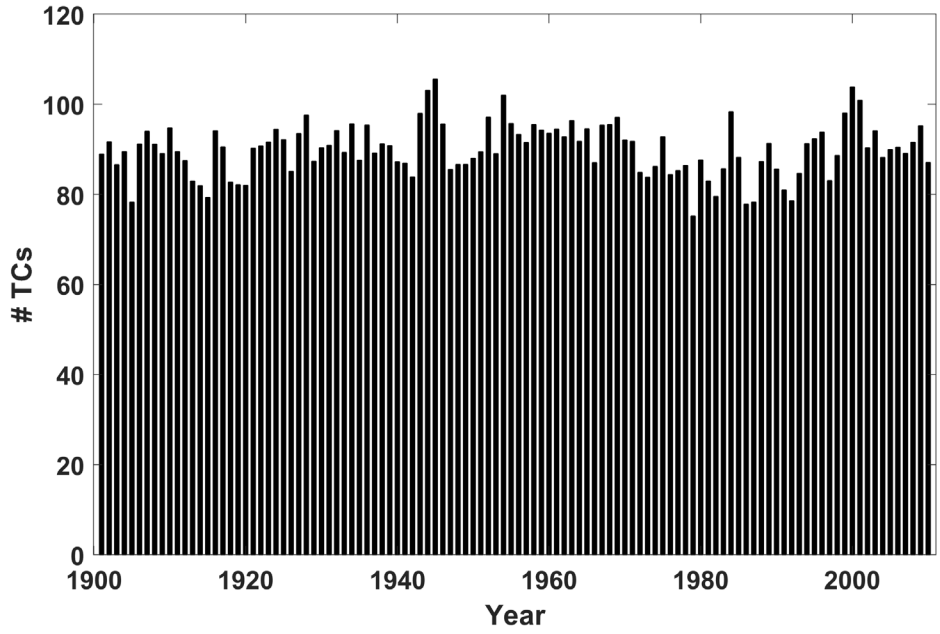

Figure 14.15: Globally and annually summed monthly genesis potential index (GPI) given by (14.4) and driven by CERA-20C reanalysis data, 1901-2010. The mean is 90 (by calibration to post-1980 observations) and the variance is 34, about 38% of what would be expected from a pure Poisson process.

14.2.2 "TC-World" Experiments

We have seen that environmental wind shear is detrimental to tropical cyclogenesis and development, and that most if not all real tropical cyclones are initiated by pre-existing disturbances that do not operate (principally or at all) through surface flux feedbacks. What happens when neither wind shear nor potential triggering disturbances are present?

One way to explore this issue is to find out what happens on a conceptually infinite $f-$plane with imposed, uniform sea surface temperature and calculated radiative transfer; in other words, RCE on an $f-$plane. This is been accomplished by extending the numerical framework used to explore self-aggregation of convection (Chapter 3, section 3.4) by including a constant Coriolis parameter. Much has been learned from this approach, which was pioneered by Bretherton et al. (2005). These have come to be known as "TC-world" experiments.

We have emphasized all along that tropical cyclones are surface flux-driven phenomenon, and that while phase change of water alters the intensity and structure of cyclones, it is not necessary to the phenomenon itself. Simulations of dry tropical cyclones were described in Chapter 9. This leads us to ask: Under what conditions do tropical cyclone-like vortices develop, as opposed to rotating convective structures typical of classical Rayleigh-Bénard convection (Emanuel 1994)?

The classical approach to understanding convection began with experiments by Henri Bénard (Bénard 1900) and was first treated theoretically, through linear stability analysis, by Lord Rayleigh (Rayleigh 1916). The approach considers the development of convection in a Boussinesq fluid between two rigid plates of infinite extent, the lower of which has a higher temperature than the upper. There is an extensive literature on this approach but little intersection between this community and the those who study atmospheric convection. Almost all the laboratory and theoretical studies of Rayleigh-Bénard convection consider aerodynamically smooth boundaries through which the fluxes of heat and momentum are always constrained by molecular diffusivities. Even with very strong thermal forcing, the solutions still depend on these diffusivities. By contrast, atmospheric boundary layer theory (e.g. Monin-Obukhov similarity (Monin and Obukhov 1954); see Chapter 4) ignores molecular diffusivities from the start, assuming that the lower boundary is aerodynamically rough. This difference between smooth and rough boundaries has divided the group of scientists studying convection into two essentially non-communicating groups for many decades.

Rotation was eventually added to the set-up (Chandrasekhar 1953, 1961). The upshot of these laboratory, theoretical, and eventually numerical studies, is that when the temperature difference between the two plates (or else the imposed heat flux through the boundary) exceeds a critical value, the system becomes linearly unstable and convection begins in the form of horizontally periodic cells. (The critical value depends on the imposed temperature difference or heat flux, the distance between the boundaries, the molecular diffusivities of heat and momentum, and the Coriolis parameter. These can be combined into three non-dimensional numbers that govern the behavior of the system.)

Under most circumstances, with fixed temperature boundaries, the aspect ratio of the convection is around unity – the horizontal distance between updrafts and downdrafts is on the order of the depth of the fluid. With background rotation, and with relatively weak thermal forcing, the updrafts are cyclonic in the lower half of the fluid and anticyclonic above that; and

vice-versa for the downdrafts. The spacing of these vortices remains on the order of the depth of the fluid. If the thermal forcing is sufficiently large to result in a highly turbulent flow, and if the rotation rate is high enough, domain-filling cyclones develop (e.g. Guervilly et al. 2014), but unlike tropical cyclones, these have height-invariant structure and are apparently driven by a local inverse cascade of energy from the convective-scale vortices, has had been envisioned by Montgomery et al. (2006) for tropical cyclones.

On the other hand, when the heat flux rather than the temperature itself is prescribed at the boundaries, the convective cells can become much broader than they are deep. And when the boundaries are permitted to be aerodynamically rough, so that mechanical turbulence limits the heat flux near the boundaries, the resulting convection can be of quite different character.

Recently, Velez-Pardo and Cronin (2023) explored the character of numerical simulations of Rayleigh-Bénard convection under different combinations of thermal boundary conditions, including fixed temperature, flixed heat flux, and aerodynamic fluxes. (They did not consider phase change of water.) Their findings are summarized in Figure 14.16.

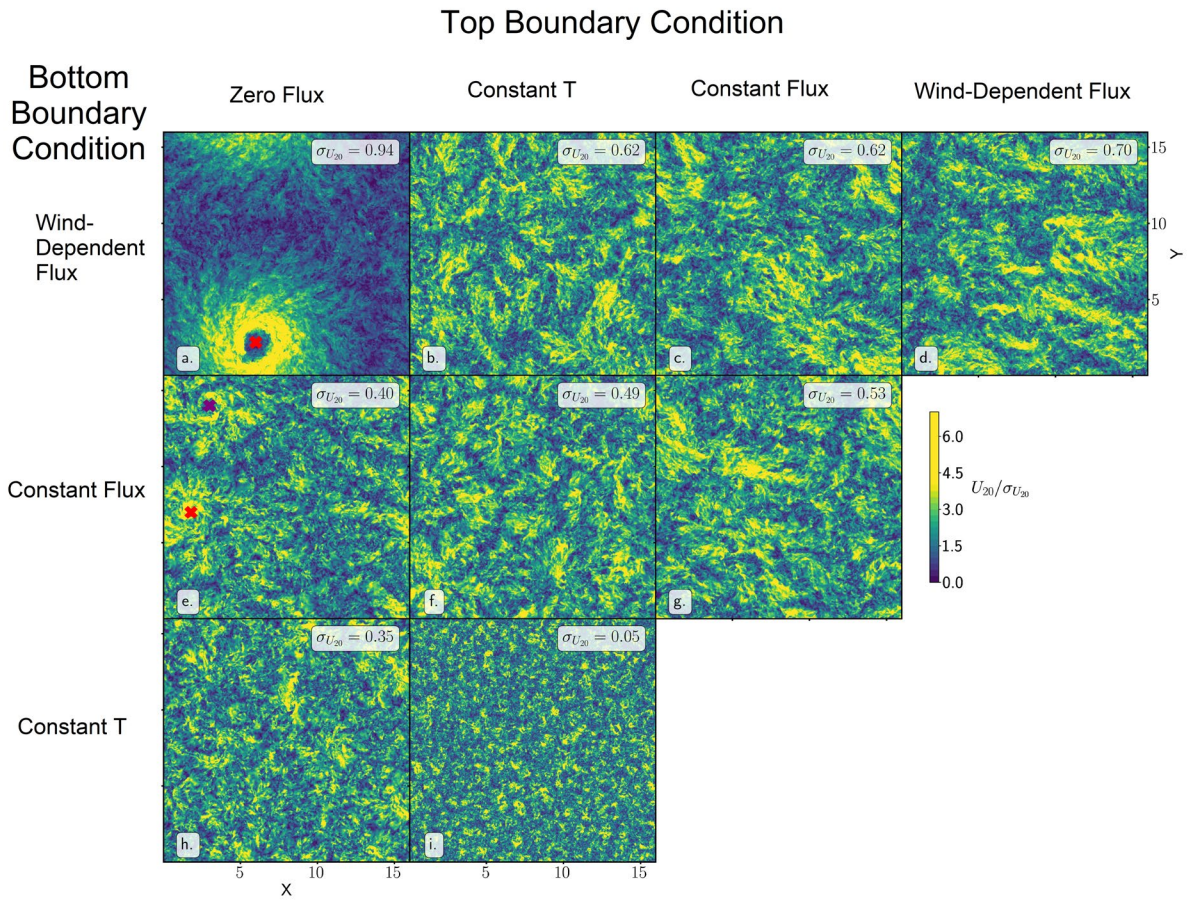

Figure 14.16: Horizontal wind at 20 percent of domain height for simulations with moderate Coriolis parameter. These snapshots were taken after 10 rotational periods into the simulations. Magnitudes are normalized by the standard deviation in each domain, and color shades saturate at 3.5 times the standard deviation. Rows represent different bottom thermal boundary conditions and columns are top boundary condition. Locations of near-surface pressure minima corresponding to persistent cyclonic vortices are indicated with "x" markers. Horizontal distances are in multiples of the fluid depth.

The figure shows snapshots of wind speed normalized by its domain-wide standard deviation at an elevation that is 20% of the domain depth, for a set of simulations in which the thermal forcing is sufficient to produce states with moderate to strong turbulence, and for a nondimensional measure of the Coriolis parameter to be moderate (see Velez-Pardo and Cronin 2023 for details). The snapshots are taken 10 rotational periods after initialization. Thermal boundary conditions are calculated by fixing the boundary temperature, fixing the boundary heat flux, or applying the aerodynamic flux formula (4.15), which depends on flow speed near the boundary, among other things. The type of boundary condition applied to the lower boundary is specified along the left side of Figure 14.16, while the top boundary condition is shown along the top. Note that for the combinations of zero flux at the top boundary and either constant flux or aerodynamic flux at the bottom boundary, the domain-mean temperature increases linearly in time. This is isomorphic to the case where we specify a constant, domain-mean heat sink in the interior of the fluid, somewhat like radiative cooling in RCE.

In all cases, no-slip boundary conditions are applied to the horizontal momentum equations. Only the upper left diagonal of the boundary condition matrix is shown because the model equations are invariant to changing the sign of the vertical coordinate and the temperature perturbation together.

For the classical fixed-temperature boundary conditions at both boundaries used by Rayleigh (1916), the separation between convective elements is about 1 fluid depth. When at least one of the two boundaries has either fixed thermal flux or uses the aerodynamic formula, the convection cells are somewhat broader than they are deep, by roughly a factor of 5.

No long-lived vortices are apparent in the fields except in the case of zero flux at the top boundary and either constant flux or aerodynamic flux at the bottom boundary. The latter case is equivalent to what most most TC-world simulations specify….no heat flux through the top of the domain and aerodynamic heat fluxes at the bottom, with (an implied) constant cooling applied through the interior. Only in this case do we see genuinely TC-like vortices emerge. The domain used here, in combination with other parameters, is only large enough to contain a single vortex in this case, but Cronin and Chavas (2019) showed that the separation distance between vortices (in their completely dry case) seems to scale as potential intensity divided by Coriolis parameter.

The use of aerodynamic flux conditions at the lower boundary is consistent with Monin-Obukhov boundary layer similarity theory (see Chapter 4) but are almost never used in theoretical or laboratory studies of Rayleigh-Bénard convection. This explains why the scientific communities that study Rayleigh-Bénard convection and tropical cyclones have remained largely independent.

This work shows that tropical cyclone-like vortices develop over aerodynamically rough boundaries in fluids for which surface thermodynamic disequilibrium is maintained by interior cooling. Phase change of water, though it has strong quantitative effects on vortex structure and intensity, is not necessary and is not the physics that truly distinguishes TC-like vortices from other forms of convection in rotating fluids.

With this background, we next turn to TC-world experiments with full radiation, phase change of water, and some representation of microphysical processes. Most of these have used convection-permitting models in which the convection is explicitly but crudely resolved, and have been run in doubly periodic or spherical domains with fixed or variable Coriolis parameter and specified, mostly constant, SSTs. The models are usually initialized by adding low-amplitude white noise to one or more model variables in a state that is otherwise at rest. Often the model is initially run in a domain that is too small to permit self-aggregation, so as to achieve something like classical RCE with random convection. Then the final state of such a simulation is unfolded into a larger domain (see Robe and Emanuel 1996 for details of this technique) and the integration is carried on in the large domain.

An example of a rotating self-aggregation experiments in a doubly periodic domain with constant Coriolis parameter and SST is the work of Wing et al. (2016). They ran the System for Atmospheric Modeling (SAM; Khairoutdinov and Randall 2003) in a *1536 km x 1536 km* domain with *3 km* horizontal grid spacing and *64* levels, with a fixed, constant SST of *305 K* and a Coriolis parameter of $5 \times 10^{-5}\ s^{-1}$. They initialized their simulations with average fields that resulted from averaging the last 20 days of a simulation over a much smaller *288 km x 288 km* domain, adding very small amplitude ($< 0.1\ K$) thermal noise to the lowest 5 levels of the domain. They ran 5 ensemble members, differing only in the particular realization of random noise in the initial conditions. Tropical cyclones spontaneously emerge in these simulations. The time evolution of the domain-maximum horizontal wind speed is shown in Figure 14.17 for each of the 5 ensemble members.

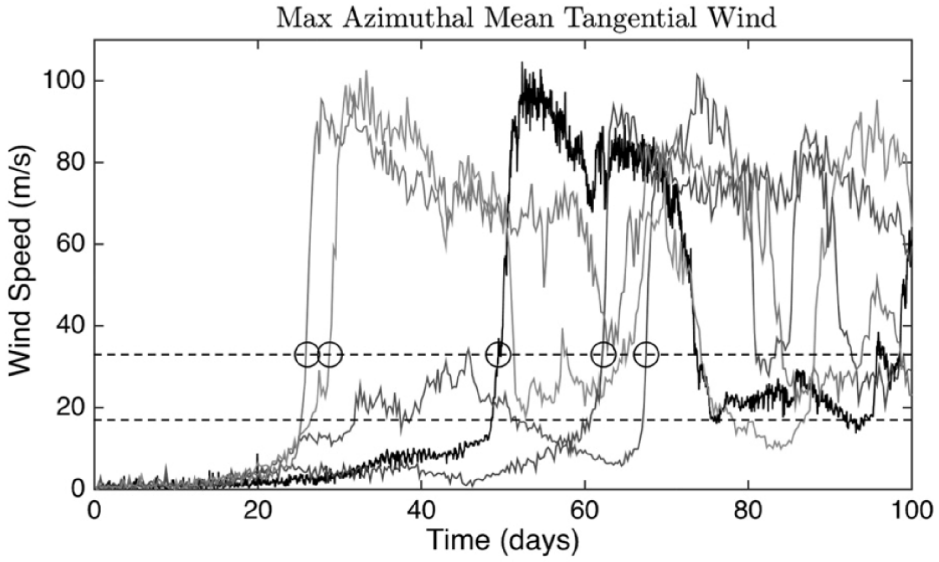

Figure 14.17: Evolution with time of the domain-maximum horizontal wind (ms^{-1}) for each of the 5 ensemble members in the rotating self-aggregation experiments performed by Wing et al. (2016).

After a gestation period ranging from about 25 to about 65 days, rapid cyclogenesis occurs. This time scale, which is longer than the observed lifetime of moist tropical cyclones, is about the time scale for the moist static energy to increase to saturation in a column in which outgoing longwave radiation has been mostly shut down by dense high clouds but surface enthalpy flux continues at its average rate. Other similar studies found similar gestation time scales and sensitivity to initial noise. This simulation resulted in only a single tropical cyclone in the doubly periodic domain, for the particular value of the Coriolis parameter used. Note in Figure 14.17 that the cyclones often collapse after 20 days or so, perhaps because they are being confined to a domain that is too small; this behavior is not observed in simulations with many tropical cyclones.

As in observational studies and many other simulations of genesis, a cold-core mid-level cyclone develops ahead of the surface cyclogenesis (Carstens and Wing 2020). Unlike in the simulations by Davis (2015), the mid-level vortex forms as a single entity in the Wing et al. (2016) simulations, again possibly because of the limited domain size.

How does spontaneous genesis occur in TC-World models? It turns out that the process is pretty much the same as occurs in the self-aggregation of non-rotating convection, described in detail in Chapter 3 section 3.4, but with a larger role for surface enthalpy flux feedback. Recall that we diagnosed the physics of self-aggregation using an equation for the variance of column-integrated moist static energy, (3.85), which we repeat here for convenience:

$$\frac{1}{2}\frac{\partial \overline{\hat{h}'^2}}{\partial t} = \overline{\hat{h}' F_{r0}'} - \overline{\hat{h}' F_{rt}'} + \overline{\hat{h}' F_{t0}'} + \overline{G\hat{\omega}'\hat{h}'}, \tag{14.6}$$

where $\hat{h}'$ is the fluctuation of column-integrated moist static energy, F_{r0} and F_{rt} are the upward radiative fluxes at the surface and tropopause, respectively, F_{t0} is the surface turbulent enthalpy flux (equivalent to the moist static energy flux), and G is the gross moist stability, which we assume to be positive. The overbars represent horizontal averages over distances that span many clouds. For the variance of column-integrated moist static energy to increase, the terms on the right side of (1.46) must sum to a positive result. Wing et al. (2016) calculated the terms in (14.6) in their simulations, dividing the radiative terms into shortwave and longwave components, with the results shown here in Figure 14.18.

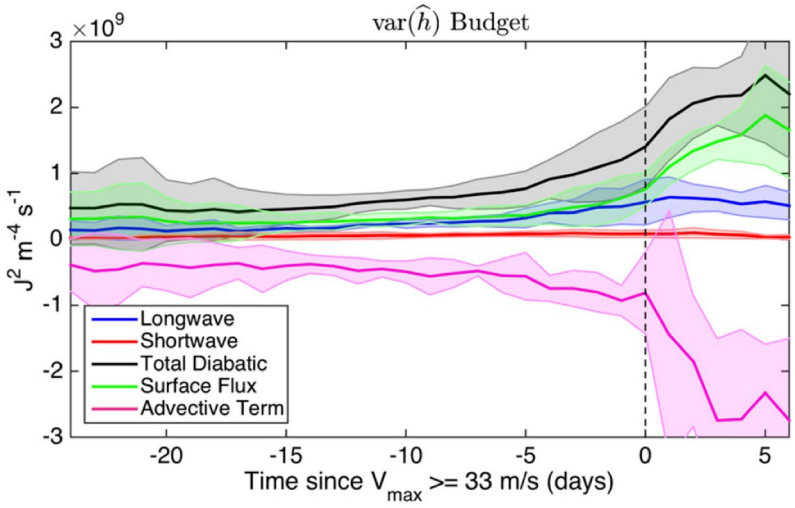

Figure 14.18: Evolution over time of the terms on the right side of (14.6). All 5 ensemble members are used, and composited with respect to the time that the wind speed first reaches hurricane intensity (33 m s^{-1}; see circles in Figure 14.17). The curves represent the ensemble mean and the shading indicates the standard deviation. The sum of the radiative and surface enthalpy flux terms is given in black; these are divided into longwave radiation (blue), shortwave radiation (red), and surface enthalpy flux (green). The advective term, a more complete version of the last term in (14.6), is shown in magenta.

It is clear from the variance budget that variance growth is owing to surface enthalpy fluxes and longwave radiation, which is likely owing mostly to high, dense clouds, as has been shown to be the case with non-rotating, self-aggregating convection. Late in the process, the surface flux feedback becomes dominant, as expected, but the longwave feedback remains positive and substantial. (In the non-rotating case, the surface flux feedback ultimately becomes negative.)

As shown by Muller and Romps (2018), when both radiative and surface flux feedbacks are suppressed, no spontaneous genesis occurs. Suppressing just the radiative feedback allows genesis to occur, but the timing is delayed and the cyclones do not become quite as strong. Cyclones can develop with radiative feedbacks only, but intensification is slower and the final intensity is considerably reduced.

Radiative feedback has been shown to accelerate the intensification phase of tropical cyclones in both TC-World simulations (Wing et al. 2016; Muller and Romps 2018) and in some real-world simulations using WRF (Ruppert et al. 2020).

Based on the non-convection-permitting, large-domain (*20,000 km x 20,000 km*) simulations by Held and Zhou (2008), which demonstrated that tropical cyclones become smaller and more densely packed as the Coriolis parameter is increased, Khairoutdinov and Emanuel (2013) performed convection-permitting simulations in a smaller domain but with an artificially inflated value of the Coriolis parameter. Specifically, they used a value of f of $5\times10^{-4}s^{-1}$ in a domain that was *2500 km* by *2500 km* with *3 km* horizontal grid spacing and *64* vertical levels. Their simulations were initialized from vertical soundings taken from a 100-day integration of a non-rotating version of the same model (SAM; Khairoutdinov and Randall 2003) in a much smaller (*96 km x 96 km*) domain, too small to allow for aggregation. This initialization procedure was applied for each SST used in the experiments. Small amplitude thermal noise was then added to the fields to initiate convection in the larger domain.

In these simulations, genesis occurred spontaneously after more than 60 days, a bit longer than the average in other studies of rotating self-aggregation (as shown in Figure 14.17). With the much larger Coriolis parameter, between 8 and 26 cyclones fill the doubly periodic domain, depending on other externally imposed conditions such as SST.

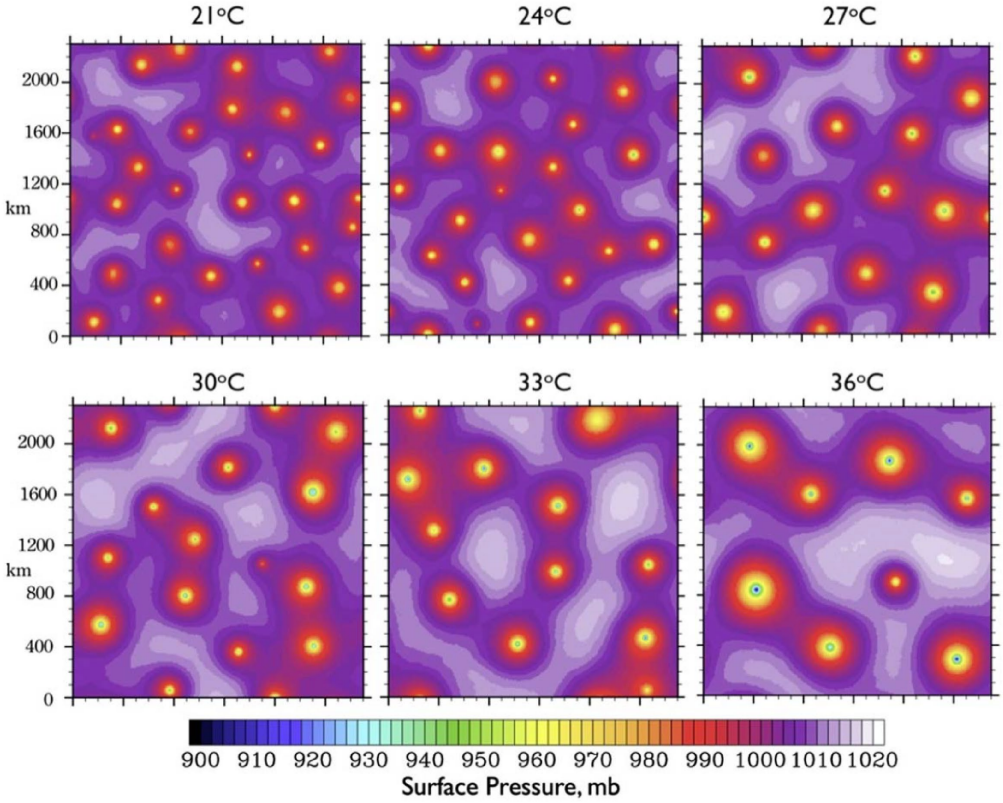

Figure 14.19: Snapshots of surface pressure taken after statistical equilibrium is reached in six experiments that differ only in the imposed sea surface temperature, as shown at the top of each panel.

Figure 14.19 shows snapshots of surface pressure for six different values of the imposed SST. These snapshots were made after statistical equilibrium was reached in each simulation. The intensity, as measured by minimum central pressure, and the diameter of the cyclones clearly increase with SST, and their number falls off correspondingly.

Enough simulations were performed to develop and evaluate scaling laws for the characteristics of tropical cyclones in the statistical equilibrium state. First, there is a clear relationship between cyclone diameter and the number of cyclones, N, since the cyclones seem to be densely packed:

$$N \simeq \frac{L^2}{D^2}, \tag{14.7}$$

where L is the length of the (square) domain and D is a characteristic distance between cyclone centers. Because it is easy to count cyclones, we will take (14.7) to be the working definition of D.

We next assume that in TC World, in contrast to the real world, the main source of irreversible entropy production is dissipation of kinetic energy in the boundary layer. If we define r_0 as a characteristic radius inside which most of the dissipation occurs, then the domain-average dissipation in the Carnot limit is

$$C_D V_p^3 \rho_a \frac{r_o^2}{D^2} \sim \varepsilon \dot{Q} = \varepsilon (F_{rt} - F_{r0}), \tag{14.8}$$

where C_D is the drag coefficient, ρ_a is the surface air density, V_p is the potential intensity (which we assume is the characteristic azimuthal velocity scale for TCs), F_{rt} is the net upward radiative flux at the top of the troposphere, F_{r0} is the net upward radiative flux at the surface, and ε is the modified thermodynamic efficiency defined

$$\varepsilon \equiv \frac{T_s - T_{cool}}{T_{cool}}, \tag{14.9}$$

where T_s is the surface air temperature and T_{cool} is now the inverse of the mean inverse temperature at which radiative cooling occurs in the system. The right-hand side is the Carnot production of mechanical energy, accounting also for dissipative heating, and the left-hand side is the average dissipation of kinetic energy.

We will test the hypothesis that the radius r_o inside of which most of the dissipation occurs scales linearly with the cyclone separation scale D:

$$r_o = \gamma D, \tag{14.10}$$

where γ is a constant which, on geometric grounds we assume obeys $0 < \gamma < 1$. If this turns out to be true, then (14.8) can be written

$$C_D \rho_a V_p^3 \gamma^2 \sim \varepsilon \dot{Q} = \varepsilon (F_{rt} - F_{r0}), \tag{14.11}$$

For the six simulations performed at different SSTs by Khairoutdinov and Emanuel (2013), Table 14.1 lists the equilibrium number of cyclones, the potential intensity based on domain mean atmospheric temperature and SST, the domain-mean kinetic energy of the lowest model level winds, the net radiative cooling, $F_{rt} - F_{r0}$, and the value of γ calculated from (14.11) assuming that $C_D = 1.5 \times 10^{-3}$, $\rho_a = 1\ Kg\ m^{-3}$, and $\varepsilon = 0.3$. (We will discuss the parameter α in due course.)

Table 14.1: TC World Statistics

SST (ºC)	21	24	27	30	33	36
# Cyclones	26	22	15	14	12	8
V_p (m s^{-1})	52.6	55.7	58.6	61.5	62.6	63.8
KE (J m^{-2})	0.34	0.38	0.43	0.45	0.46	0.49
$F_{rt} - F_{r0}\ \left(W\,m^{-2}\right)$	92.7	102.7	112.7	120.1	128.1	136.8
γ	0.36	0.34	0.33	0.32	0.32	0.32
$\alpha\ \left(\times 10^3\right)$	0.84	0.83	0.92	0.87	0.86	0.96

Note that γ is nearly constant, with a mean value of about 0.334. Using this mean value in (14.11) yields a regression coefficient of 0.99 between the predicted and actual values of the potential intensity. Also, as expected, the surface kinetic energy is highly correlated with the square of the potential intensity, also with a regression coefficient of 0.99.

Consequently, (14.11) tells us that the strength of the cyclones in TC World is proportional to the cube root of the rate of radiative cooling of the system, and is inversely proportional to the cube root of the drag coefficient. The horizontal scale of the cyclones seems to vary linearly with the separation distance between cyclones, but that does not tell us what this separation distance is. To estimate that, we bring in two further constraints. The first constraint is that the mean rate of latent heat release in the rain areas of the cyclones must equal to the rate of radiative cooling:

$$ML_v \Delta q^* = F_{rt} - F_{r0}, \tag{14.12}$$

where M is the updraft mass flux, L_v is the latent heat of vaporization, and Δq^* is the difference between the saturation specific humidity at cloud base and at cloud top. We next make two approximations to (14.12). First, we assume that q^* at cloud top is essentially zero, given the very cold temperature at the tops of the cyclones. We also assume that q^* at cloud base equals the actual value of specific humidity in the boundary layer, q_b, and in turn assume that the latter is the saturation specific humidity at SST and mean surface pressure p_0, multiplied by a near-surface relative humidity, which we take to be 0.8. Taken together, we are assuming that

$$\Delta q^* \simeq q_b \simeq 0.8 q^*(SST, p_0). \tag{14.13}$$

We can write the updraft mass flux as the product of air density ρ, updraft velocity w, and the fractional area σ occupied by the rainy cores of the cyclone:

$$M = \rho \sigma w. \tag{14.14}$$

From the Ekman radial velocity equation, (9.83), together with mass continuity, we can show that the vertical velocity in steady axisymmetric cyclone scales as

$$w \sim C_D V_p. \tag{14.15}$$

Combining (14.12) – (14.15) yields an expression for the fractional area:

$$\sigma \simeq \frac{F_{rt} - F_{r0}}{\rho C_D V_p L_v q_b}. \tag{14.16}$$

We next eliminate $F_{rt} - F_{r0}$ between (14.16) and (14.11):

$$\sigma = \frac{\gamma^2 V_p^2}{\varepsilon L_v q_b} \tag{14.17}$$

Note that although the potential intensity V_p increases with SST, it does not do so as rapidly as q^* and so (14.17) predicts that the fraction area occupied by the rainy cores of the cyclones decreases with increasing SST.

Finally, we represent the fractional area covered by the rainy areas as

$$\sigma = \frac{r_r^2}{D^2}, \tag{14.18}$$

where r_r is the radius of the rain area. We next make an ansatz which rests on rather scant evidence, which is that the inner core radius r_r equals $\alpha V_p / f$. where α is a numerically small nondimensional number. Combining this with (14.18) and (14.17) yields

$$D^2 = \frac{\alpha^2 \varepsilon L_v q_b}{f^2 \gamma^2}. \tag{14.19}$$

Using (14.7), this also gives us an estimate of the storm count:

$$N = \frac{L^2 f^2 \gamma^2}{\alpha^2 \varepsilon L_v q_b}. \tag{14.20}$$

Using the storm counts in Table 14.1 together with the specified domain length L, Coriolis parameter f, the mean value of γ form Table 14.1, and q_b from (14.13) and the SSTs in Table (14.1), we use (14.20) to calculate the value of α listed in Table 14.1. Although α does vary from 0.83×10^{-3} to 0.96×10^{-3}, it does not vary systematically with SST.

If we use the six-experiment mean values of α and γ from Table 14.1, we can summarize what we believe to be the correct scaling laws for $f-$ ***plane*** TC Worlds in statistical equilibrium:

$$V_p = \left(9 \frac{\varepsilon (F_{rt} - F_{r0})}{C_D \rho_a} \right)^{1/3}, \tag{14.21}$$

$$\sigma = 0.14 \frac{V_p^2}{\varepsilon L_v q_{SST}^*}, \tag{14.22}$$

$$D = 2.5 \frac{\sqrt{\varepsilon L_v q_{SST}^*}}{f}, \tag{14.23}$$

$$N = 0.18 \frac{L^2 f^2}{\varepsilon L_v q_{SST}^*}, \tag{14.24}$$

where q_{SST}^* is the saturation specific humidity at sea surface temperature and pressure.

We note that a somewhat better fit between predicted and simulated potential intensity can be obtained by modifying (14.21) to include a threshold:

$$V_p = \left(13.5 \frac{\varepsilon (F_{rt} - F_{r0})}{C_D \rho_a} - 1 \times 10^5 m^3 s^{-3} \right)^{1/3}, \tag{14.25}$$

with the provision that V_p cannot be negative. This may imply that a threshold level of thermodynamic disequilibrium between the surface and the atmosphere is required for organization into tropical cyclones. This is consistent with the work of Ilya Prigogine (Nicolis and Prigogine 1977), who argued that a finite degree of thermodynamic disequilibrium is necessary for self-organized structures to emerge, and is also consistent with some empirical genesis indices, such as that given by (14.4), which have a threshold potential intensity for tropical cyclone formation. Likewise, in their dry simulations, Velez-Pardo and Cronin (2023) found that large-scale persistent vortices in the case of a lower aerodynamic boundary condition only develop when a nondimensional measure of the thermal forcing (the convective Rossby Number) is large enough.

In their simulations using a global model with 25 km grid spacing but with constant SST and Coriolis parameter, Reed and Chavas (2015) found that the outer structure of their simulated vortices closely matches the prediction of the theoretical outer wind structure predicted by (9.84). A dimensional analysis of (9.84) reveals that if we again assume that the radii of maximum winds scale as $V_p / f,$ then the outer radius, which should define the storm spacing in equilibrium must obey

$$D = \frac{V_p}{f} F\left(\frac{C_D V_p}{w_e} \right), \tag{14.26}$$

where F is some nondimensional function. Moreover, from clear sky energy balance,

$$w_e = \frac{F_{rt} - F_{r0}}{\rho L_v q_b}. \tag{14.27}$$

It can easily be shown that if F is just the square root function, then (14.26) and (14.27) lead to (14.23). Indeed, it can be shown that the solution to (9.84) in the limit of large $C_D V_p / w_e$ gives an F that asymptotically approaches a square root function. Thus, provided $C_D V_p / w_e$ is large, the spacing of cyclones in TC-World is also consistent with the outer wind field given by (9.84) for a radius of maximum winds that scales at V_p / f.

The scaling law (14.25) tells us that cyclone intensity increases slowly with temperature and eventually saturates in RCE. It saturates because there is an upper bound on $F_{rt} - F_{r0}$ in RCE, for which F_{rt} vanishes (no net radiative flux at the top of the atmosphere) and, in very infrared-opaque atmospheres, F_{r0} is effectively bounded by the surface solar flux, since strange things happen when the net surface infrared flux becomes negative.

The fractional area covered by the rainy cores of the cyclone decreases with increasing temperature, according to (14.22), because the saturation specific humidity increases faster than the square of the potential intensity.

Finally, the number of cyclones per unit area drops rapidly with increasing temperature, according to (14.24), consistent with Figure 14.19. The storms become larger, however, and the net power dissipation increases slowly, along with the net radiative cooling of the atmosphere, as expressed by (14.11). In the real world, damage from tropical cyclones tends to increase with roughly the cube of the wind speed, and of course large storms will cause more damage than

smaller ones, all other things being equal. Consequently, if there were structures to damage in TC World, that damage would increase slowly with temperature.

In statistical equilibrium, the domain-average rain rate is constrained so that the net latent heat release balances the radiative cooling of the cloud layer. As shown in Table 14.1, this cooling rate, proportional to $F_{rt} - F_{r0}$, increases slowly with SST. On the other hand, the peak rainfall rate scales as wq_b, where w is a characteristic upward velocity in the storm core. Using the Ekman scaling (14.15), this means that the peak rain rates should scale as $C_D V_p q_b$. Peak rain rates rise even faster than Clausius-Clapeyron, because V_p also increases with SST.

The rapid increase of the maximum rain rate together with the slow increase of domain-average rainfall with SST is consistent with the decrease of the fractional area covered by the storm cores implied by (14.22) and observed in TC-World experiments.

Several variants on the original rotating RCE experiments have emerged in recent years. While most such experiments continue to be performed with fixed SSTs, a few have replaced those with shallow slab oceans (e.g. Zhou et al. 2017; Viale and Merlis 2017). In these simulations, the water underneath the eyewall cools in response to cloud shading and enhanced surface enthalpy flux because of strong winds. Eventually a new equilibrium is reached with less sunlight warming the surface under the cyclones' cores, and, owing to locally depressed SST, less enthalpy flux into the atmosphere. Yet the balance between Carnot cycle energy generation and surface kinetic energy dissipation, embodied in (14.11), still seems to hold, and because the net radiative cooling of the system is not very different from the fixed SST case, the power dissipation is also roughly the same.

Several simulations have been performed on constant SST aqua-planets (Shi and Bretherton 2014; Reed and Chavas 2015; Merlis et al. 2016; Chavas and Reed 2019; Walsh et al. 2020; Vu et al. 2021), and most of these have allowed the Coriolis parameter to vary with latitude (Shi and Bretherton 2014; Merlis et al. 2016; Chavas and Reed 2019; Walsh et al. 2020; Vu et al. 2021). The upshot is that β drift (see Chapter 12 section 12.1.3) causes cyclones to drift westward and toward higher latitudes. Shi and Bretherton (2014) showed that while these cyclones last for 60-120 days (unlike the doubly periodic f-plane where they last as long as the simulation runs), they eventually break up near the poles, perhaps owing to baroclinic instability of the vortices themselves. (Because they are slow to adjust to the poleward-decreasing Coriolis parameter, they arrive at higher latitude with sizes somewhat larger than the local deformation radius.) The transport of momentum by these poleward-drifting cyclones leads to a weak Hadley-like circulation even though there are no horizontal temperature gradients.

In their doubly-periodic $f-$ plane simulations, Carstens and Wing (2020, 2022) showed that tropical cyclones do not develop if the Coriolis parameter is too small, though that might be partially an artifact of using a domain size too small to accommodate the natural size of tropical cyclones when the Coriolis parameter is small. But on the sphere, it is quite possible that β limits tropical cyclone formation near the equator. Chavas and Reed (2019) present persuasive evidence that tropical cyclones have difficulty developing if their diameter exceeds the Rhines scale (Rhines 1975), which is $\sqrt{U/\beta}$, where U is a characteristic velocity of the outer region of a tropical cyclone. If we assume that equilibrium tropical cyclone size varies inversely with Coriolis parameter, as indicated by (14.23), then this scale will exceed the Rhines scale

sufficiently close to the equator. Chavas and Reed argued that the maximum genesis rate will occur around the latitude where the two scales are roughly equal.

In doubly periodic $f-$ plane experiments, and to some extent in constant SST simulations on aquaplanet spheres with variable Coriolis parameter, the number of tropical cyclones at any given time is a packing problem: How many cyclones of a given diameter (say, as given by (14.23)) will fit in the domain? But when one moves away from such idealizations toward more real-world conditions, for example, models with pole-to-equator SST gradients, the problem of cyclone frequency becomes more complex. For one thing, one has to deal with environmental wind shear, not just the shears associated with the cyclones themselves. The frequency of tropical cyclones ceases to become a function of SST alone and depends on the whole pattern of SST.

Merlis et al. (2013), by imposing a hemispherically asymmetric ocean heat flux in a climate model with 50-km horizontal grid spacing, showed that the frequency of tropical cyclogenesis increases as the ITCZ is displaced further poleward. This demonstrates that for the same overall climate forcing, regionality of climate, in this case imposed through ocean heat fluxes, can strongly affect the global frequency of tropical cyclones. While, as we have seen, uniform warming of a constant SST domain always results in fewer (but larger) cyclones, Merlis et al. show that warming accompanied by a shift in ocean heat transport can lead to increases of cyclone frequency. Consequently, the spatial variability of climate is important, not just the global mean state.

We can demonstrate the importance of such processes as ocean heat transport on just the potential intensity, putting aside wind shear and atmospheric humidity for the moment.

Consider first the heat budget of a small patch of ocean mixed layer, of depth h, as illustrated in Figure 14.20.

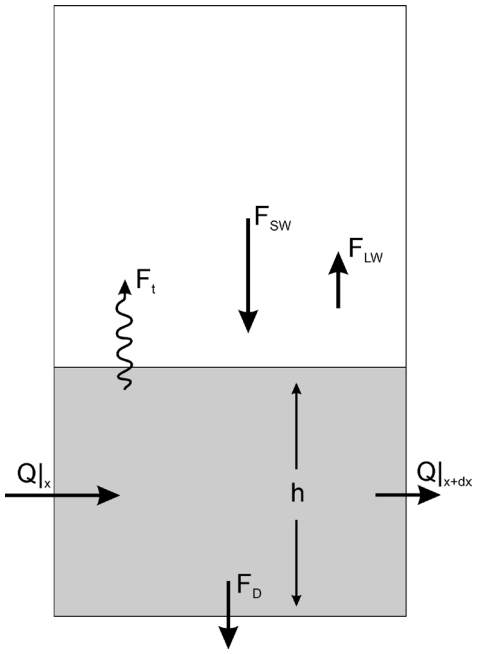

Figure 14.20: Heat budget of the ocean mixed layer (shading). The fluxes per unit area of shortwave and longwave radiation, turbulent enthalpy, and ocean mixed layer entrainment are denoted by F_{SW}, F_{LW}, F_t, and F_D, respectively. Vertically integrated lateral heat fluxes at the left and right sides of the box are $Q|_x$ and $Q|_{x+dx}$, respectively.

Assuming that the heat content of the patch of ocean mixed layer is not changing over time, the heat budget demands that

$$F_t = F_{SW} - F_{LW} - F_D - \nabla_2 \bullet \mathbf{Q} = \rho_a C_k |\mathbf{V}_a| \left(k_0^* - k_a\right), \tag{14.28}$$

where ∇_2 is the horizontal gradient operator, $\mathbf{Q}$ is the vertically integrated ocean horizontal heat flux vector, and we have used the neutral aerodynamic flux formula for F_t, with ρ_a the near-surface air density, C_k the enthalpy flux transfer coefficient, $|\mathbf{V}_a|$ the near-surface wind speed, k_0^* the saturation enthalpy of the air at SST and surface pressure, and k_a is the enthalpy of near-surface air. The fluxes per unit area of shortwave and longwave radiation, turbulent enthalpy, and ocean mixed layer entrainment are denoted by F_{SW}, F_{LW}, F_t, and F_D, respectively.

Now potential intensity is given by (9.26):

$$V_p^2 = \frac{T_b - T_o}{T_o} \frac{C_k}{C_D} \left(k_0^* - k_a\right). \tag{14.29}$$

Eliminating $C_k \left(k_0^* - k_a\right)$ between (14.29) and (14.28) yields:

$$V_p^2 = \frac{T_b - T_o}{T_o} \left(\frac{F_{SW} - F_{LW} - F_D - \nabla_2 \bullet Q}{\rho_a C_D |\mathbf{V}_a|} \right). \tag{14.30}$$

This shows that in equilibrium conditions, potential intensity is increased by increasing surface insolation, decreasing net longwave flux from the surface, decreasing detrainment of heat into the deeper ocean, increasing convergence of the vertically integrated ocean lateral heat flux, and decreasing near-surface wind speed. The assumption of a steady state is not valid over a seasonal cycle but is not too bad when averaged over a few years.

Changing turbulent heat flux, which in the tropics is carried mostly as a latent heat flux, will also influence the humidity of the lower and middle troposphere, which is an important contributor to genesis potential indices. Since, in the tropics, the convergence of the ocean heat flux is of the same magnitude as the net surface radiative flux (Trenberth and Caron 2001), it can have a strong influence on potential intensity, and through its modification of surface latent heat flux and atmospheric circulation, the humidity of the lower and middle troposphere, both of which affect tropical cyclone genesis frequency as estimated by indices such as (14.4).

Large-scale circulations in both the atmosphere and the ocean play a strong role in the climatology of tropical cyclones, circumscribing regions where such storms can form, even within the tropics, as illustrated by Figure 14.13. Perhaps the overall frequency of tropical cyclones is just a packing problem limited to these regions This hypothesis was tested by Hoogewind et al. (2020), but they found that the packing limit is about an order-of-magnitude higher than the observed frequency of cyclones, suggesting that other factors, such as the frequency of suitable triggering disturbances, may be playing a role.

In summary. the TC-World experiments have shown us that in idealized worlds with no SST gradients and therefore little or no external wind shear, tropical cyclones will develop and, unless they are too close to the equator, fill up the available space according to their diameters. But unless seeded with external triggering disturbances, the time to genesis is many tens of days – too long to develop in the real world, where disturbances would typically travel out of the area of enough genesis potential in less time than that. And, in the real world, the presence of external wind shear and the space time variability of it and other large-scale conditions (as measured by, e.g., genesis potential indices) and of triggering disturbances, strongly limits overall genesis rates.

14.2.3: Random seeding experiments

Random seeding was developed as part of an approach to estimating long-term tropical cyclone risk using physically based models. Accurate risk assessment depends, among other things, on having a sufficiently long record of events to make statistically robust estimates of hazards like wind and flooding, encompassing the all-important low-frequency tails of the probability distributions of those hazards. Analysis of damage from many different natural hazards reveals that long-term damage is dominated by events with return periods of a hundred or a few hundred years… rare enough that societies are not well adapted to them, but common enough to contribute to long-term damage. Historical records of the natural phenomena involved are rarely long enough to provide robust estimates of hazards with return periods of even 100 years. Climate change presents the additional complication of making the underlying statistics non-stationary.

On approach to making robust estimates of long-term risk is to numerically simulate many thousands of years of TCs using physically based models. At the same time, accurate numerical simulation of tropical cyclones requires grid spacings on the order of a few kilometers (Rotunno

et al. 2009). It is currently not possible to run even basin-sale models with such fine resolution for the equivalent of thousands of years.

To address this problem, a technique was developed for creating many thousands of tropical cyclone events driven by the relatively coarse output of global models and reanalyses (Emanuel et al. 2008). In the first step, the time-evolving output of such models or reanalyses is seeded randomly in space and time with weak, tropical depression-strength vortices. These are assumed to moved with a weighted vertical mean of the large-scale flow plus a $\beta-$ drift, as described in Chapter 12, section 12.1. Finally, a simple, deterministic coupled ocean-atmosphere TC model in run on each track to determine the evolution of the storm's intensity. The deterministic model, the Coupled Hurricane Intensity Forecasting System (CHIPS; Emanuel 1995), is axisymmetric but contains a parameterization of ventilation optimized to produce skillful real-time intensity forecasts (Emanuel and Rappaport 2000). It is coupled to a simple one-dimensional ocean model that incorporates the physics of storm-induced mixing of cold water to the surface. The axisymmetric model is based on quasi-balance equations written in angular momentum coordinates rather than in physical radius; this yields high spatial resolution in the core, where it is needed, with higher resolution at higher intensity.

The intensity model predicts that the vast majority of seeds perish immediately because they are in unfavorable environments. The survivors are regarded as constituting the climatology of tropical cyclones pertinent to the global model or reanalysis used to drive the procedure. The method is akin to biological natural selection, although it is more selection of those put down in favorable environments than survival of the fittest seeds.

The method has been shown to reproduce, with reasonable accuracy, the observed climatology of tropical cyclones, including their seasonal variation in each ocean basin, the probability distribution of their intensities, and their response to natural climate fluctuations like ENSO. We emphasize here that the method filters any triggering disturbances that might be present in the global model or reanalysis fields, so that the triggering used in the procedure is random, except for a dependence on latitude.

Figure 14.21 shows the results of applying this procedure to a global reanalysis (ERA5; Hersbach et al. 2020) over the years 1980-2020, in terms of the annual average numbers of tropical cyclones in each ocean basin. The rate of random seeding has been chosen to yield a reasonable global average annual number of storms. As with genesis indices, the global number must be assigned; it is not predicted by the technique (although its year-to-year variability is).

The technique performs quite well, with the important exceptions of the southwest Pacific Ocean and the eastern North Pacific region. In the latter case, the random seeding produces less than half the observed annual average number of cyclones. Danso et al. (2022) showed that in the absence of African easterly waves, North Atlantic tropical cyclones form further west than they do with AEWS are present, but at roughly the same rate. . Many eastern North Pacific tropical cyclones also develop from easterly waves (Molinari et al. 1997; Zehnder et al. 1999), but taking them away allows for precious little space for cyclones to develop from weaker noise, compared to the Atlantic case. (The distance from Dakar to Miami is about 6,500 km, whereas eastern Pacific tropical cyclones typically run out of positive genesis potential in about half that distance.) Consequently, it is possible that the frequency and characteristics of triggering disturbances plays a more important role in eastern North Pacific cyclogenesis than it does in other regions.

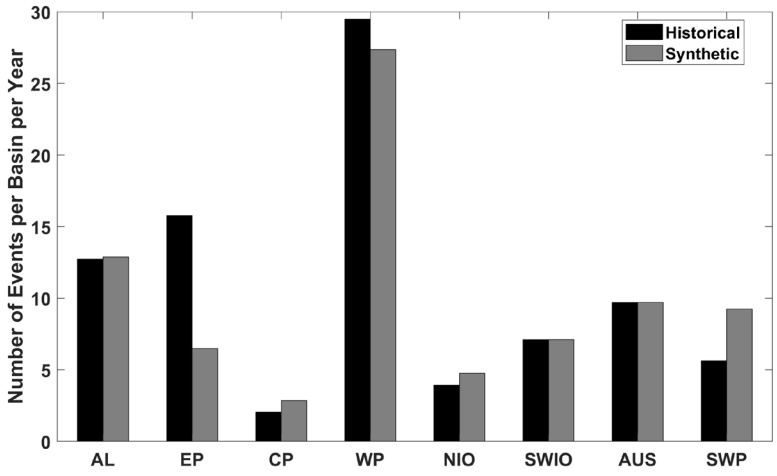

Figure 14.21: Average annual number of tropical cyclones over the period 1980-2020 in observations (IBTrACS; Knapp et al. 2010; black bars) and from random seeding (gray bars). The totals are presented for the North Atlantic (AL), eastern North Pacific (EP), central North Pacific (CP), western North Pacific (WP), North Indian Ocean (NIO), southwest Indian Ocean (SWIO), Australian region (AUS) and southwest Pacific (SWP).

14.3 Synthesis

The TC-World experiments tell us that under highly ideal conditions, tropical cyclones can develop spontaneously in RCE states owing to a combination of WISHE and radiative feedbacks. But the spontaneous emergence of cyclones takes tens of days – too long for cyclogenesis in the real world, where the background airflow would normally take growing disturbances out of favorable environments in less time. Nevertheless, these simulations and experiments conducted under more realistic conditions show that radiative feedbacks can accelerate cyclogenesis and that it is difficult if not impossible to develop tropical cyclones when both feedbacks are absent.

Case studies and numerical experiments under both idealized and real-world conditions show that tropical cyclones always (or almost always) develop out of pre-existing disturbances that originate at least somewhat independently. Field experimental studies and numerical experiments as well as theory, strongly suggest that a prerequisite for tropical cyclone development is the establishment of a nearly saturated mesoscale lower and middle troposphere above the subcloud layer. If such a region retains a nearly moist adiabatic lapse rate, it either must have a greatly elevated moist static energy or else it must be relatively cold compared to surrounding regions (or, more likely, a bit of both; see Figure 14.11). To prevent the cold anomaly from radiating away as gravity waves, it must be rotating and nearly in gradient and hydrostatic balance, which implies a mesocyclone aloft. Mesocyclones are observed along the route to genesis in many field experiments and most numerical simulations.

The experiments by Cronin and Chavas (2019) demonstrated that, for the same potential intensity, moist cyclones generally become stronger than dry cyclones. At the same time, the presence of moisture allows for a depression of mid-tropospheric moist entropy that cannot occur in a dry atmosphere with adiabatic lapse rates. Multiple lines of evidence show that such

a depression inhibits cyclogenesis and, in the presence of shear, weakens mature storms: moisture paradoxically makes storms potentially more intense and less likely. The physics of the inhibition seems to be tied to ventilation of the storm core by low moist entropy air in the lower to middle troposphere, made possible by the dynamic interaction between the TC and environmental wind shear. The nondimensional ventilation parameter, defined by (12.23), is an important parameter both for storm intensification and for mature intensity, and a similar parameter is part of many semi-empirical genesis indices like (14.4).

The early investigators of tropical cyclones, like Riehl (1951) and Dunn (1951), recognized that tropical cyclones occur when a suitable initiating disturbance occurs in a favorable environment. Between then and now we have come to understand more about what constitutes a favorable environment and physically why it is favorable, and also what makes for a suitable initiating disturbance. A remaining question is whether the observed rates of genesis are governed more by the degree of environmental salubriousness or by the frequency and character of initiating disturbances. While we have come to understand fairly well what controls the number of cyclones in idealized TC-Worlds, we also understand that observed genesis rates fall well short of expectations based on such experiments, which have little or no external wind shear.

In section 14.2.1 we reviewed the work of Patricola et al. (2018) and Danso et al. (2022) that suggested that while initiating disturbances help determine when and where genesis occurs, they do not seem to determine whether it occurs. This seems to imply that rates of genesis are more determined by the large-scale environment than by the frequency or character of initiating disturbances. This finding is also consistent with the success of genesis indices. At the same time, the long time scales needed for spontaneous genesis in highly favorable environments suggests that triggers are necessary in the real world. How do we reconcile this seeming paradox?

Here we develop a semi-quantitative conceptual framework for thinking about this problem. This framework is based on a pair of ordinary differential equations developed by the author (Emanuel 2017) for emulating the behavior of a deterministic tropical cyclone intensity model (Emanuel 1995) driven by real-world boundary conditions and used as an aid to forecasting actual storms in real time (Emanuel and Rappaport 2000). The CHIPS model is described briefly in section 14.2.3.

The emulator was designed to obey certain asymptotic limits, and in the absence of shear reduces to (10.23). It was refined and optimized against thousands of CHIPS intensity forecasts. The pair of ordinary differential equations are for two variables: the maximum gradient azimuthal wind speed, V_g, and a non-dimensional moisture variable m that varies between 0 and 1. They are as follows:

$$\frac{dV_g}{dt} = \frac{1}{2}\frac{C_D}{h}\left[\alpha\left(1-\epsilon-\kappa\right)V_p^2 m^3 - \left(1-\left(\epsilon+\alpha\kappa\right)m^3\right)V_g^2\right], \tag{14.31}$$

and

$$\frac{dm}{dt} = \frac{1}{2}\frac{C_D}{h}\left[\left(1-m\right)V_g - S\chi m\right], \tag{14.32}$$

where C_D is the drag coefficient, h is a boundary layer depth, α is an ocean-interaction parameter that varies with upper ocean properties, and various properties of the cyclone, ϵ is the raw thermodynamic efficiency:

$$\epsilon \equiv \frac{T_s - T_o}{T_s}. \tag{14.33}$$

The coefficient κ governs heating by isothermal expansion and is defined

$$\kappa \equiv \frac{\epsilon}{2} \frac{C_k}{C_D} \frac{L_v q_0^*}{R_d T_s}, \tag{14.34}$$

where T_s is the surface temperature, T_o is the tropical cyclone outflow temperature, C_k is the surface enthalpy exchange coefficient, L_v is the latent heat of vaporization, q_0^* is the surface saturation specific humidity at ambient environmental surface pressure, and R_d is the gas constant for dry air.

Finally, S is the magnitude of the 250 hPa – 850 hPa environmental wind shear, V_p is the potential intensity, and χ is a nondimensional measure of the saturation deficit of the lower to middle troposphere:

$$\chi = \frac{h_b - h_m}{h_0^* - h_b}, \tag{14.35}$$

where h_b and h_m are the moist static energies of the boundary layer and middle troposphere, and h_0^* is the saturation moist static energy of air at sea surface temperature and pressure. (Note that the χ factor was set to a constant 2.2 in Emanuel (2017)).

For our narrow purposes here, we neglect all ocean response, which entails setting $\alpha = 1$ in (14.31). While in practice, the parameters (like potential intensity and shear) vary along the tracks of tropical cyclones, we hold them constant here. We also nondimensionalize the equations by substituting nondimensional time and velocity scales:

$$\begin{aligned} t &= \frac{2h}{C_D V_p} \tau, \\ V_g &= V_p V. \end{aligned} \tag{14.36}$$

With these provisions, (14.31) – (14.32) become

$$\frac{dV}{d\tau} = \left(1 - a\right) m^3 - \left(1 - a m^3\right) V^2, \tag{14.37}$$

and

$$\frac{dm}{d\tau} = \left(1 - m\right) V - \Lambda m, \tag{14.38}$$

where

$$a \equiv \epsilon + \kappa, \tag{14.39}$$

and Λ is the ventilation parameter:

$$\Lambda \equiv \frac{S\chi}{V_p}. \tag{14.40}$$

We also hold a constant in this exercise.

We examine the behavior of the system comprised of (14.37) and (14.38). A detailed mathematical analysis of the system has been presented by Slyman et al. (2023).

First, depending on the value of the ventilation parameter Λ, (14.37) and (14.38) have either one real steady-state solution, or three. These are shown for the velocity V by the thick, black curves in Figure 14.22 for the case $a = 0.47$.

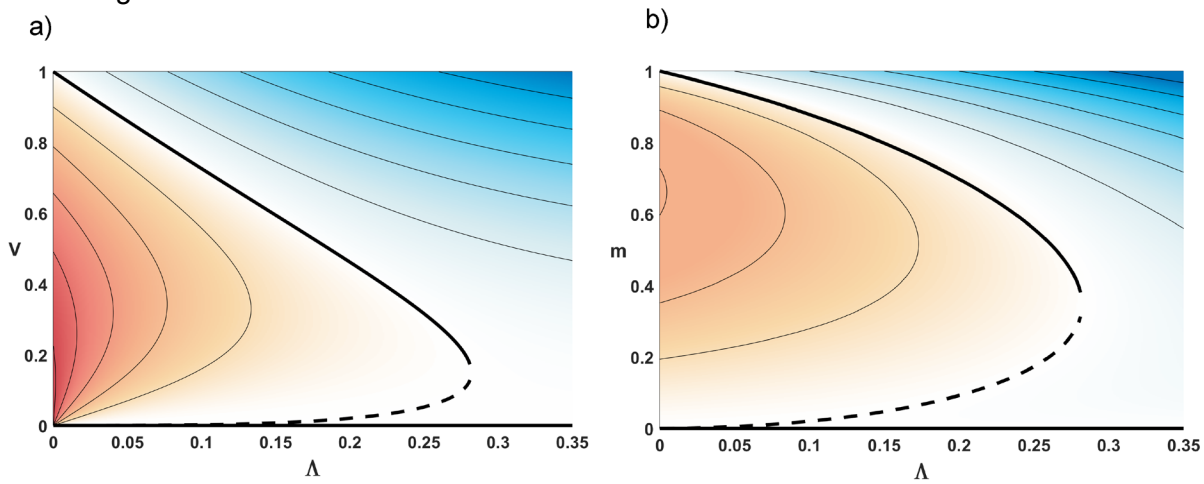

Figure 14.22: Regime diagrams for (14.37) and (14.38). The thick black curves show the steady state solutions for the nondimensional a) wind speed V and b) moisture variable m as functions of the ventilation parameter, Λ. Solid curves show stable states, and the dashed curves are unstable steady states. The colors and thin contours show a) the time rate of change of V for the special case that m is in a quasi-steady-state (nullcline of m), and b) the time rate of change of m for the special case that V is in a quasi-steady-state (nullcline of V) with warm colors denoting growth and cool colors denoting decay.

The state of no cyclone, $V = 0,\ m = 0,$ is always linearly stable, although through much of the range of ventilation parameter, it does not take much positive perturbation of V (but somewhat more of m) to tip the system into unstable growth. The shape of the steady-state solutions in 14.21a somewhat resemble the solutions of the system explored by Brian Tang (Tang 2010; Tang and Emanuel 2010) presented in Chapter 12, section 12.2 and graphed in Figures 12.16 and 12.17, but differ in details.

While the steady state solutions shown by the black curves in Figure 14.22 are universal, we show time rates-of-change of V and m for the special cases that the other variable is quasi-steady, which we obtain by setting the time derivative to zero in either (14.37) or (14.38). (In general, the evolutions of V and m depend on their initial values; the time rates-of-change shown in Figure 14.21 are not universal.)

In the special case of no shear ($\Lambda = 0$), the resting state is unstable and, in general, weak disturbances will grow slowly, depending on the initial values of V and m. In general, the growth of the cyclone is somewhat more sensitive to initial moisture than to initial velocity. This is illustrated by Figure 14.23, which shows the time evolution of wind speed for different values of initial wind speed for an initial moisture $m = 0$ (a), and for initial values of moisture given a weak initial vortex $V = 0.05$ (b).

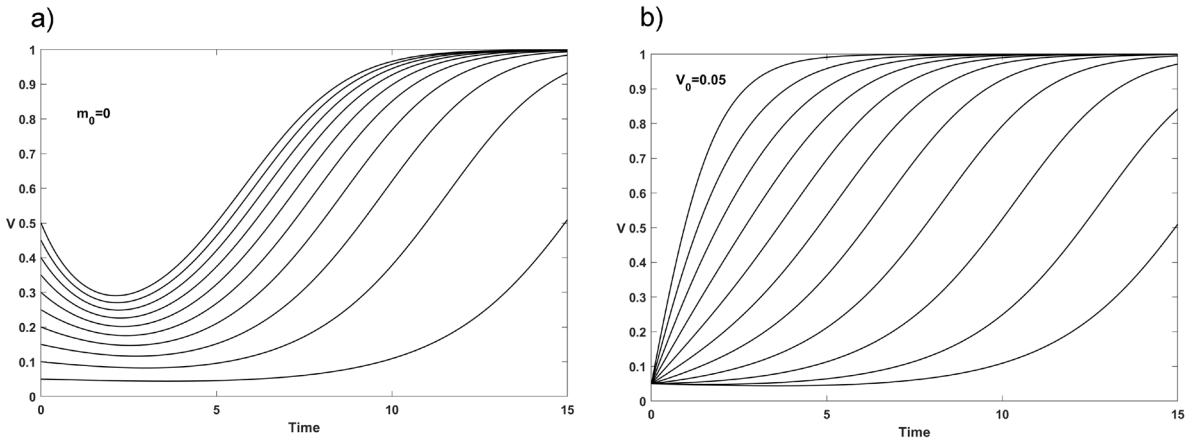

Figure 14.23: Evolution with nondimensional time of the nondimensional wind speed for a) zero initial moisture perturbation and initial winds speeds of from 0.05 to 1 in increments of 0.05, and b) initial wind speed of 0.05 for varying initial moisture perturbation from 0 to 1 in increments of 0.1. The velocity is normalized by potential intensity and one nondimensional time unit is approximately equal to 1 day. The ventilation parameter is zero in these integrations.

In the absence of any initial moisture perturbation, cyclones take a long time to develop. A weak disturbance ($V = 0.05$, Figure 4.23a) takes more than 10 time units (about 10 days) to develop, and strong initial vortices initially decay before finally amplifying, not reaching peak wind speed until about 10 time units. By contrast, even a weak disturbance will amplify quite rapidly with a large initial moisture perturbation (Figure 14.23b).

The effect of moderate ventilation on the evolution of disturbances is shown in Figure 14.24. Given a weak initial vortex, only perturbations with strong moisture anomalies amplify appreciably within 15 time units, and, consistent with Figure 14.22, disturbances amplify to a steady state well below the potential intensity. The initial vortex with the strongest moisture anomaly ($m = 1$) slightly overshoots the steady-state intensity before settling down.

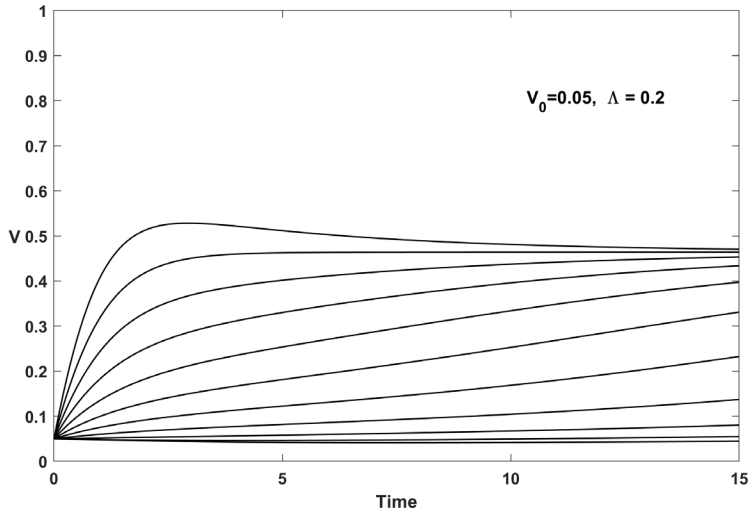

Figure 14.24: As in Figure 14.22 b but for a case with moderate shear ($\Lambda = 0.2$).

Using these results, we propose a conceptual framework for understanding tropical cyclogenesis based on the bifurcation diagram shown in Figure 14.22b. We choose to work in $m - \Lambda$ space because development is more sensitive to the initial values of m than to V. The conceptual framework is illustrated by Figure 14.25. Weather noise in the nondimensional moisture variable m moves the initial point in the diagram vertically, while noise in the nondimensional ventilation parameter moves the state horizontally. Together, they produce a joint probability distribution that is continuously explored by weather noise. The two probability distributions, and their joint probability, vary with location, season, and climate state. When the noise extends far enough into the upper left portion of the bifurcation diagram, and stays there long enough, a tropical cyclone will develop.

One might think of the moisture variable m as being associated with triggering disturbances and the ventilation parameter Λ as associated with the synoptic-scale environment. If the ventilation parameter frequently resides in the region of growth, then genesis frequency will be mostly sensitive to the frequency and amplitude of disturbances in the moisture variable m. On the other hand, if moisture disturbances frequently inhabit the region of strong growth, the overall frequency would be more determined by the probability distribution of Λ. The success of genesis indices and random seeding argues strongly in favor of the latter circumstance, except possibly in the eastern North Pacific region.

Finally, we have tacitly assumed that the probability distributions of triggering and ventilation are independent from each other and from the climatology of the tropical cyclones themselves. Yet there is growing evidence that this not the case, because tropical cyclones may dry out the tropical atmosphere, increasing lower to middle tropospheric saturation deficit (χ) and thereby increasing the ventilation parameter Λ, and may also alter ocean heat transport. These issues are tackled in Chapter 15.

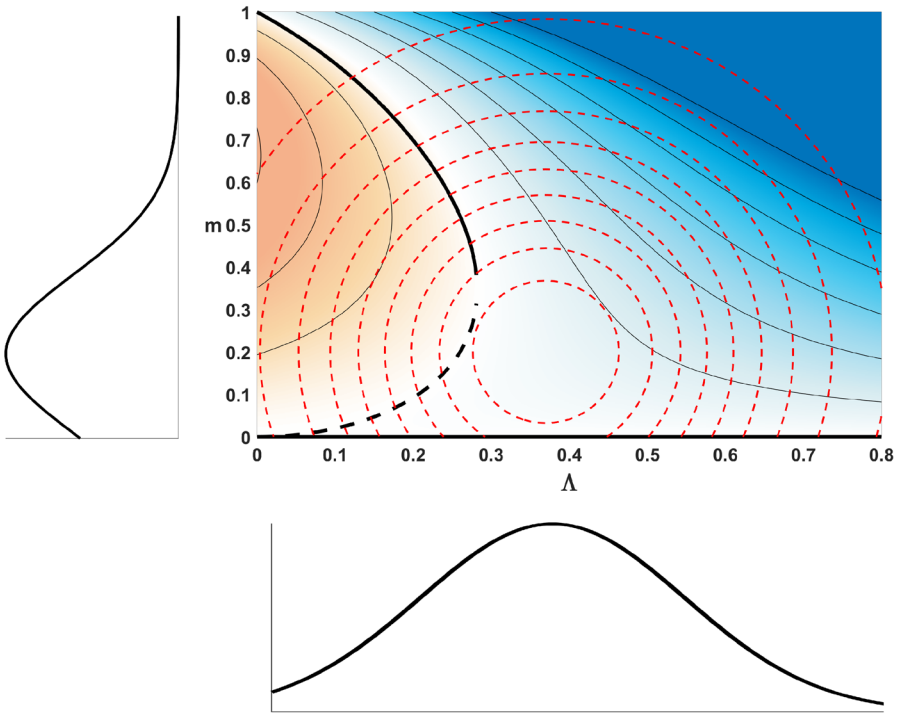

Figure 14.25: Illustrating the genesis conceptual framework based on the bifurcation diagram of Figure 14.21b. The panels at the left and bottom show probability distributions of weather noise in the nondimensional moisture variable m and ventilation parameter Λ, and the dashed red contours in the center panel show their joint probability.

References

Bartels, D. L., and and R. A. Maddox, 1991: Midlevel cyclonic vortices generated by mesoscale convective systems. *Mon. Wea. Rev*, 119.

Bénard, H., 1900: Étude expérimentale des courants de convection dans une nappe liquide. — Régime permanent : tourbillons cellulaires. *J. Phys. Theor. Appl.*, **9**, 513–524, https://doi.org/10.1051/jphystap:019000090051300.

Bergeron, T., 1954: The problem of tropical hurricanes. *Quart. J. Roy. Meteor. Soc.*, **80**, 131–164.

Bister, M., and K. A. Emanuel, 1997: The genesis of Hurricane Guillermo: TEXMEX analyses and a modeling study. *Mon. Wea. Rev.*, **125**, 2662–2682.

Bister, M. H., 1996: Development of tropical cyclones from mesoscale convective systems. Massachusetts Institute of Technology, 112 pp. https://dspace.mit.edu/handle/1721.1/57851.

Bosart, L. F., and F. Sanders, 1981: The Johnstown Flood of July 1977: A Long-Lived Convective System. *Journal of the Atmospheric Sciences*, **38**, 1616–1642, https://doi.org/10.1175/1520-0469(1981)038<1616:tjfoja>2.0.co;2.

Bosart, L. F., and J. A. Bartlo, 1991: Tropical storm formation in a baroclinic environment. *Mon. Wea. Rev.*, **119**, 1979–2013.

Braun, S. A., J. A. Sippel, and D. S. Nolan, 2012: The impact of dry midlevel air on hurricane intensity in idealized simulations with no mean flow. *Journal of the Atmospheric Sciences*, **69**, 236–257, https://doi.org/10.1175/jas-d-10-05007.1.

Bretherton, C. S., P. N. Blossey, and M. F. Khairoutdinov, 2005: An energy-balance analysis of deep convective self-aggregation above uniform SST. *J. Atmos. Sci.*, **62**, 4273–4292.

Bruyère, C. L., G. J. Holland, and E. Towler, 2012: Investigating the use of a genesis potential index for tropical cyclones in the North Atlantic basin. *Journal of Climate*, **25**, 8611–8626, https://doi.org/10.1175/jcli-d-11-00619.1.

Camargo, S., 2013: Global and regional aspects of tropical cyclone activity in the CMIP5 models. *J. Climate*, **26**, 9880–9902.

Camargo, S. J., K. A. Emanuel, and A. H. Sobel, 2007a: Use of a genesis potential index to diagnose ENSO effects on tropical cyclone genesis. *J Climate*, **20**, 4819–4834, https://doi.org/10.1175/Jcli4282.1.

——, A. H. Sobel, A. G. Barnston, and K. A. Emanuel, 2007b: Tropical cyclone genesis potential index in climate models. *Tellus A*, **59**, 428–443, https://doi.org/10.1111/j.1600-0870.2007.00238.x.

——, M. C. Wheeler, and A. H. Sobel, 2009: Diagnosis of the MJO Modulation of Tropical Cyclogenesis Using an Empirical Index. *J Atmos Sci*, **66**, 3061–3074, https://doi.org/10.1175/2009jas3101.1.

Carstens, J. D., and A. A. Wing, 2020: Tropical cyclogenesis from self-aggregated convection in numerical simulations of rotating radiative-convective equilibrium. *Journal of Advances in Modeling Earth Systems*, **12**, e2019MS002020, https://doi.org/10.1029/2019MS002020.

——, and ——, 2022: A spectrum of convective self-aggregation based on background rotation. *Journal of Advances in Modeling Earth Systems*, **14**, e2021MS002860, https://doi.org/10.1029/2021MS002860.

Chandrasekhar, S., 1953: Problems of stability in hydrodynamics and hydromagnetics: George Darwin lecture, delivered by Professor s. Chandrasekhar on 1953 Novemher 13. *Monthly Notices of the Royal Astronomical Society*, **113**, 667–678, https://doi.org/10.1093/mnras/113.6.667.

——, 1961: Hydrodynamic and Hydromagnetic Stability. Oxford University Press, New York. *654 pp.*,.

Charney, J. G., and A. Eliassen, 1964: On the growth of the hurricane depression. *J. Atmos. Sci.*, **21**, 68–75.

Chavas, D. R., and K. A. Reed, 2019: Dynamical aquaplanet experiments with uniform thermal forcing: System dynamics and implications for tropical cyclone genesis and size. *Journal of the Atmospheric Sciences*, **76**, 2257–2274, https://doi.org/10.1175/JAS-D-19-0001.1.

Cronin, T. W., and D. R. Chavas, 2019: Dry and Semidry Tropical Cyclones. *Journal of the Atmospheric Sciences*, **76**, 2193–2212, https://doi.org/10.1175/jas-d-18-0357.1.

Danso, D. K., C. M. Patricola, and E. Bercos-Hickey, 2022: Influence of African easterly wave suppression on Atlantic tropical cyclone activity in a convection-permitting model. *Geophysical Research Letters*, **49**, e2022GL100590, https://doi.org/10.1029/2022GL100590.

Davis, C. A., 2015: The formation of moist vortices and tropical cyclones in idealized simulations. *Journal of the Atmospheric Sciences*, **72**, 3499–3516, https://doi.org/10.1175/JAS-D-15-0027.1.

Dunkerton, T. J., M. T. Montgomery, and Z. Wang, 2008: Tropical cyclogenesis in a tropical wave critical layer: easterly waves. *Atmospheric Chemistry and Physics Discussions*, **8**, 11149–11292.

Dunn, G. E., 1940: Cyclogenesis in the tropical Atlantic. *Bulletin of the American Meteorological Society*, **21**, 215–229.

——, 1951: Tropical Cyclones. *Compendium of Meteorology*, T.F. Malone, Ed., American Meteorological Society, 887–901.

Emanuel, K., 2010: Tropical cyclone activity downscaled from NOAA-CIRES reanalysis, 1908-1958. *J. Adv. Model. Earth Sys.*, **2**, 1–12.

——, 2013: Downscaling CMIP5 climate models shows increased tropical cyclone activity over the 21st century. *Proc. Nat. Acad. Sci.*, **110**, 12219–12224, https://doi.org/10.1073/pnas.1301293110.

——, 2017: A fast intensity simulator for tropical cyclone risk analysis. *Nat. Hazards*, https://doi.org/10.1007/s11069-017-2890-7.

Emanuel, K., 2020: Response of Global Tropical Cyclone Activity to Increasing CO2 : Results from Downscaling CMIP6 Models. *Journal of Climate*, **34**, 57–70, https://doi.org/10.1175/jcli-d-20-0367.1.

Emanuel, K., and E. Rappaport, 2000: Forecast skill of a simplified hurricane intensity prediction model. Preprints of the 24th Conf. Hurricanes and Trop. Meteor., Ft. Lauderdale, FL, Amer. Meteor. Soc., Boston, 236–237.

——, R. Sundararajan, and J. Williams, 2008: Hurricanes and global warming: Results from downscaling IPCC AR4 simulations. *Bull. Amer. Meteor. Soc.*, **89**, 347–367.

Emanuel, K. A., 1989: The Finite-Amplitude Nature of Tropical Cyclogenesis. *Journal of the Atmospheric Sciences*, **46**, 3431–3456, https://doi.org/10.1175/1520-0469(1989)046<3431:tfanot>2.0.co;2.

Emanuel, K. A., 1994: *Atmospheric Convection*. Oxford Univ. Press, New York, 580 pp.

——, 1995: The behavior of a simple hurricane model using a convective scheme based on subcloud-layer entropy equilibrium. *J. Atmos. Sci.*, **52**, 3959–3968.

——, and D. S. Nolan, 2004: Tropical cyclone activity and the global climate system. *26th AMS Conference on Hurricanes and Tropical Meteorology*,.

Espy, J. P., 1841: *The Philosophy of Storms*. Little and Brown,.

Gray, W. M., 1975: *Tropical cyclone genesis*.

——, 1979: Hurricanes: Their formation, structure, and likely role in the tropical circulation. *Meteorology over the tropical oceans*, D.B. Shaw, Ed., Roy. Meteor. Soc., 155–218.

Guervilly, C., D. W. Hughes, and C. A. Jones, 2014: Large-scale vortices in rapidly rotating Rayleigh–Bénard convection. *Journal of Fluid Mechanics*, **758**, 407–435, https://doi.org/10.1017/jfm.2014.542.

von Hann, J., 1901: *Lehrbuch der Meteorologie (Textbook of Meteorology)*. C. H. Tauchnitz, 847 pp.

Hawkins, H. F., and D. T. Rubsam, 1968: Hurricane Hilda, 1964. I: Genesis, as revealed by satellite photographs, conventional and aircraft data. *Mon. Wea. Rev.*, **96**, 428–452.

Held, I., and M. Zhao, 2008: Horizontally homogeneous rotating radiative-convective equilibria at GCM resolution. *J. Atmos. Sci.*, **65**, 2003–2013.

Hersbach, H., and Coauthors, 2020: The ERA5 global reanalysis. *Quarterly Journal of the Royal Meteorological Society*, **146**, 1999–2049, https://doi.org/10.1002/qj.3803.

Hoogewind, K. A., D. R. Chavas, B. A. Schenkel, and M. E. O'Neill, 2020: Exploring controls on tropical cyclone count through the geography of environmental favorability. *Journal of Climate*, **33**, 1725–1745, https://doi.org/10.1175/JCLI-D-18-0862.1.

Hsieh, T.-L., G. A. Vecchi, W. Yang, I. M. Held, and S. T. Garner, 2020: Large-scale control on the frequency of tropical cyclones and seeds: a consistent relationship across a hierarchy of global atmospheric models. *Climate Dynamics*, **55**, 3177–3196, https://doi.org/10.1007/s00382-020-05446-5.

Khairoutdinov, M. F., and D. A. Randall, 2003: Cloud resolving modeling of the ARM summer 1997 IOP: Model formulation, results, uncertainties and sensitivities. *J. Atmos. Sci.*, **60**, 607–625.

——, and K. Emanuel, 2013: Rotating radiative-convective equilibrium simulated by a cloud-resolving model. *J. Adv. Model. Earth Sys.*, **5**, 816–825.

Kilroy, G., R. K. Smith, and M. T. D.-:10. 1002/qj. 2934 Montgomery, 2017: A unified view of tropical cyclogenesis and intensification. *Quarterly Journal of the Royal Meteorological Society*, **143**, 450–462.

Knapp, K. R., M. C. Kruk, D. H. Levinson, H. J. Diamond, and C. J. Neumann, 2010: The International Best Track Archive for Climate Stewardship (IBTrACS): Unifying tropical cyclone best track data. *Bull. Amer. Meteor. Soc.*, **91**, 363–376.

Korty, R. L., S. J. Camargo, and J. Galewsky, 2012a: Tropical cyclone genesis factors in simulations of the last glacial maximum. *Journal of Climate*, **25**, 4348–4365, https://doi.org/10.1175/jcli-d-11-00517.1.

——, ——, and ——, 2012b: Variations in tropical cyclone genesis factors in simulations of the Holocene epoch. *Journal of Climate*, **25**, 8196–8211, https://doi.org/10.1175/jcli-d-12-00033.1.

Laloyaux, P., and Coauthors, 2018: CERA-20C: A Coupled Reanalysis of the Twentieth Century. *Journal of Advances in Modeling Earth Systems*, **10**, 1172–1195, https://doi.org/10.1029/2018MS001273.

Merlis, T. M., M. Zhao, and I. M. Held, 2013: The sensitivity of hurricane frequency to ITCZ changes and radiatively forced warming in aquaplanet simulations. *Geophysical Research Letters*, **40**, 4109–4114, https://doi.org/10.1002/grl.50680.

——, W. Zhou, I. M. Held, and M. Zhao, 2016: Surface temperature dependence of tropical cyclone-permitting simulations in a spherical model with uniform thermal forcing. *Geophysical Research Letters*, **43**, 2859–2865, https://doi.org/10.1002/2016GL067730.

Molinari, J., S. Skubis, and D. Vollaro, 1995: External influences on hurricane intensity. Part III: Potential vorticity structure. *Journal of Atmospheric Sciences*, **52**, 3593–3606, https://doi.org/10.1175/1520-0469(1995)052<3593:EIOHIP>2.0.CO;2.

——, D. Knight, M. Dickinson, D. Vollaro, and S. Skubis, 1997: Potential vorticity, easterly waves, and eastern Pacific tropical cyclogenesis. *Monthly Weather Review*, **125**, 2699–2708, https://doi.org/10.1175/1520-0493(1997)125<2699:PVEWAE>2.0.CO;2.

——, D. Vollaro, and K. L. Corbosiero, 2004: Tropical cyclone formation in a sheared environment: a case study. *Journal of the Atmospheric Sciences*, **61**, 2493–2509, https://doi.org/10.1175/jas3291.1.

Monin, A. S., and A. M. Obukhov, 1954: Basic laws of turbulent mixing in the surface layer of the atmosphere. *Tr. Akad. Nauk. SSSR Geophiz. Inst.*, **24**, 163–187.

Montgomery, M. T., and J. Enagonio, 1998: Tropical cyclogenesis via convectively forced vortex Rossby waves in a three-dimensional quasigeostrophic model. *J. Atmos. Sci.*, **55**, 3176–3207.

——, and R. K. Smith, 2012: The genesis of Typhoon Nuri as observed during the Tropical Cyclone Structure 2008 (TCS08) field experiment. Part 2: Observations of the convective environment. *Atmos. Chem. Phys.*, **12**, 4001–4009, https://doi.org/10.5194/acp-12-4001-2012.

——, M. E. Nicholls, T. A. Cram, and A. B. Saunders, 2006: A vortical hot tower route to tropical cyclogenesis. *Journal of the Atmospheric Sciences*, **63**, 355–386, https://doi.org/10.1175/jas3604.1.

Montgomery, M. T., and Coauthors, 2012: The pre-depression investigation of cloud-systems in the tropics (PREDICT) experiment: Scientific basis, new analysis tools, and some first results. *Bulletin of the American Meteorological Society*, **93**, 153–172, https://doi.org/10.1175/bams-d-11-00046.1.

Mrowiec, A. A., S. T. Garner, and O. M. Pauluis, 2011: Axisymmetric hurricane in a dry atmosphere: Theoretical framework and numerical experiments. *J. Atmos. Sci.*, **68**, 1607–1619.

Muller, C. J., and D. M. Romps, 2018: Acceleration of tropical cyclogenesis by self-aggregation feedbacks. *Proceedings of the National Academy of Sciences*, **115**, 2930–2935, https://doi.org/10.1073/pnas.1719967115.

Nicolis, G., and I. Prigogine, 1977: *Self-organization in nonequilibrium systems*. John Wiley & Sons, 490 pp.

Nolan, D. S., 2007: What is the trigger for tropical cyclogenesis? *Aust. Met. Mag.*, **56**, 241–266.

Nolan, D. S., and E. D. D.-:10. 1029/2008GL034147 Rappin, 2008: Increased sensitivity of tropical cyclogenesis to wind shear in higher SST environments. *Geophysical Research Letters*, **35**.

Nolan, D. S., and M. G. McGauley, 2012: Tropical cyclogenesis in wind shear: Climatological relationships and physical processes. *Cyclones: Formation, Triggers, and Control*, K. Oouchi and H. Fudeyasu, Eds., Nova Science Publishers.

Nolan, D. S., E. D. Rappin, and K. A. D.-:10. 1002/qj. 170 Emanuel, 2007: Tropical cyclogenesis sensitivity to environmental parameters in radiative–convective equilibrium. *Quarterly Journal of the Royal Meteorological Society*, **133**, 2085–2107.

Ooyama, K., 1964: A dynamical model for the study of tropical cyclone development. *Geofis. Int.*, **4**, 187–198.

Palmén, E., 1948: On the formation and structure of tropical hurricanes. *Geophysica*, **3**, 26–39.

Patricola, C. M., R. Saravanan, and P. D.-:10. 1002/2017GL076081 Chang, 2018: The response of Atlantic tropical cyclones to suppression of African easterly waves. *Geophysical Research Letters*, **45**, 471–479.

Pauluis, O., and I. M. Held, 2002: Entropy budget of an atmosphere in radiative-convective equilibrium. Part I: Maximum work and frictional dissipation. *J. Atmos. Sci.*, **59**, 125–139.

Ramage, C. S., 1959: Hurricane development. *Journal of Meteorology*, **16**, 227–237, https://doi.org/10.1175/1520-0469(1959)016<0227:hd>2.0.co;2.

Rappin, E. D., D. S. Nolan, and K. A. D.-:10. 1002/qj. 706 Emanuel, 2010: Thermodynamic control of tropical cyclogenesis in environments of radiative-convective equilibrium with shear. *Quarterly Journal of the Royal Meteorological Society*, **136**, 1954–1971.

Rayleigh, L. (John W. S., 1916: On convective currents in a horizontal layer of fluid when the higher temperature is on the underside. *Phil. Mag.;*, **32**, 529-546.

Raymond, D. J., S. L. Sessions, and C. L. D.-:10. 1029/2011JD015624 Carrillo, 2011: Thermodynamics of tropical cyclogenesis in the northwest Pacific. *Journal of Geophysical Research: Atmospheres*, **116**.

Reed, K. A., and D. R. Chavas, 2015: Uniformly rotating global radiative-convective equilibrium in the Community Atmosphere Model, version 5. *Journal of Advances in Modeling Earth Systems*, **7**, 1938–1955, https://doi.org/10.1002/2015MS000519.

Reilly, D. H., 1992: On the role of upper-tropospheric potential vorticity advection in tropical cyclone formation: Case studies from 1991. Massachusetts Institute of Technology, 124 pp. https://dspace.mit.edu/handle/1721.1/54988.

Rhines, P. B., 1975: Waves and turbulence on a beta-plane. *Journal of Fluid Mechanics*, **69**, 417–443, https://doi.org/10.1017/S0022112075001504.

Riehl, H., 1948a: *On the formation of west Atlantic hurricanes*.

Riehl, H., 1948b: On the formation of typhoons. *Journal of Meteorology*, **5**, 247–265, https://doi.org/10.1175/1520-0469(1948)005<0247:otfot>2.0.co;2.

——, 1951: Aerology of Tropical Storms. *Compendium of Meteorology*, T.F. Malone, Ed., American Meteorological Society, 902–913.

Riehl, H., 1954: *Tropical Meteorology*. McGraw-Hill, 392 pp.

——, 1963: Some relations between wind and thermal structure of steady state hurricanes. *J. Atmos. Sci.*, **20**, 276–287.

——, 1975: *Further studies on the origin of hurricanes*. Colorado State Univ.,.

Robe, F. R., and K. Emanuel, 1996: Dependence of tropical convection on radiative forcing. *J. Atmos. Sci.*, **53**, 3265–3275.

Rotunno, R., and K. A. Emanuel, 1987: An air-sea interaction theory for tropical cyclones. Part II. *J. Atmos. Sci.*, **44**, 542–561.

——, Y. Chen, W. Wang, C. Davis, J. Dudhia, and C. L. Holland, 2009: Large-eddy simulation of an idealized tropical cyclone. *Bull. Amer. Meteor. Soc.*, **90**, 1783–1788.

Ruppert, J. H., A. A. Wing, X. Tang, and E. L. Duran, 2020: The critical role of cloud–infrared radiation feedback in tropical cyclone development. *Proceedings of the National Academy of Sciences*, **117**, 27884–27892, https://doi.org/10.1073/pnas.2013584117.

Sadler, J. C., 1967: *The tropical upper tropospheric trough as a secondary source of typhoons and a primary source of tradewind disturbances*. Hawaii Institute of Geophysics,.

——, 1976a: *Tropical cyclone initiation by the tropical upper tropospheric trough*. Naval Environmental Prediction Research Facility,.

Sadler, J. C., 1976b: A role of the tropical upper tropospheric trough in early season typhoon development. *Monthly Weather Review*, **104**, 1266–1278, https://doi.org/10.1175/1520-0493(1976)104<1266:AROTTU>2.0.CO;2.

Shi, X., and C. S. Bretherton, 2014: Large-scale character of an atmosphere in rotating radiative-convective equilibrium. *Journal of Advances in Modeling Earth Systems*, **6**, 616–629, https://doi.org/10.1002/2014MS000342.

Simpson, R. H., N. FRANK, D. SHIDELER, and H. M. JOHNSON, 1968: Atlantic tropical disturbances, 1967. *Monthly Weather Review*, **96**, 251–259, https://doi.org/10.1175/1520-0493(1968)096<0251:ATD>2.0.CO;2.

Skamarock, W. C., and Coauthors, 2019: A description of the advanced research WRF version 4. *NCAR tech. note ncar/tn-556+ str*, **145**.

Slyman, K., J. A. Gemmer, N. K. Corak, C. Kiers, and C. K. R. T. Jones, 2023: Tipping in a low-dimensional model of a tropical cyclone.

Sugi, M., Y. Yamada, K. Yoshida, R. Mizuta, M. Nakano, C. Kodama, and M. Satoh, 2020: Future Changes in the Global Frequency of Tropical Cyclone Seeds. *SOLA*, **16**, 70–74, https://doi.org/10.2151/sola.2020-012.

Tang, B., and K. Emanuel, 2010: Midlevel ventilation's constraint on tropical cyclone intensity. *Journal of the Atmospheric Sciences*, **67**, 1817–1830, https://doi.org/10.1175/2010jas3318.1.

Tang, B. H.-An., 2010: Midlevel ventilation's constraint on tropical cyclone intensity. Massachusetts Institute of Technology, Department of Earth, Atmospheric, and Planetary Sciences, 195 pp. https://dspace.mit.edu/handle/1721.1/62321.

Thorncroft, C., and K. Hodges, 2001: African easterly wave variability and its relationship to atlantic tropical cyclone activity. *Journal of Climate*, **14**, 1166–1179, https://doi.org/10.1175/1520-0442(2001)014<1166:AEWVAI>2.0.CO;2.

Tippett, M. K., S. Camargo, and A. H. Sobel, 2011: A Poisson regression index for tropical cyclone genesis and the role of large-scale vorticity in genesis. *J. Climate*, **24**, 2335–2357.

Trenberth, K. E., and J. M. Caron, 2001: Estimates of Meridional Atmosphere and Ocean Heat Transports. *Journal of Climate*, **14**, 3433–3443.

Vecchi, G. A., and Coauthors, 2019: Tropical cyclone sensitivities to CO2 doubling: roles of atmospheric resolution, synoptic variability and background climate changes. *Climate Dynamics*, **53**, 5999–6033, https://doi.org/10.1007/s00382-019-04913-y.

Velez-Pardo, M., and T. W. Cronin, 2023: Large-scale circulations and dry tropical cyclones in direct numerical simulations of rotating Rayleigh-Bénard convection. *J. Atmos. Sci.*, In press.

Viale, F., and T. M. Merlis, 2017: Variations in tropical cyclone frequency response to solar and CO2 forcing in aquaplanet simulations. *Journal of Advances in Modeling Earth Systems*, **9**, 4–18, https://doi.org/10.1002/2016MS000785.

Vu, T.-A., C. Kieu, D. Chavas, and Q. Wang, 2021: A numerical study of the global formation of tropical cyclones. *Journal of Advances in Modeling Earth Systems*, **13**, e2020MS002207, https://doi.org/10.1029/2020MS002207.

Walsh, K. J. E., S. Sharmila, M. Thatcher, S. Wales, S. Utembe, and A. Vaughan, 2020: Real world and tropical cyclone world. part ii: sensitivity of tropical cyclone formation to uniform and meridionally varying sea surface temperatures under aquaplanet conditions. *Journal of Climate*, **33**, 1473–1486, https://doi.org/10.1175/JCLI-D-19-0079.1.

Wang, Z., M. T. Montgomery, and T. J. Dunkerton, 2010: Genesis of pre–Hurricane Felix (2007). Part I: The role of the easterly wave critical layer. *Journal of the Atmospheric Sciences*, **67**, 1711–1729, https://doi.org/10.1175/2009jas3420.1.

——, M. T. Montgomery, and C. Fritz, 2012: A First Look at the Structure of the Wave Pouch during the 2009 PREDICT–GRIP Dry Runs over the Atlantic. *Monthly Weather Review*, **140**, 1144–1163, https://doi.org/10.1175/mwr-d-10-05063.1.

Wing, A. A., S. J. Camargo, and A. H. Sobel, 2016: Role of radiative–convective feedbacks in spontaneous tropical cyclogenesis in idealized numerical simulations. *Journal of the Atmospheric Sciences*, **73**, 2633–2642, https://doi.org/10.1175/JAS-D-15-0380.1.

Zehnder, J. A., D. M. Powell, and D. L. Ropp, 1999: The interaction of easterly waves, orography, and the intertropical convergence zone in the genesis of eastern Pacific tropical cyclones. *Monthly Weather Review*, **127**, 1566–1585, https://doi.org/10.1175/1520-0493(1999)127<1566:TIOEWO>2.0.CO;2.

Zehr, R. M., 1992: *Tropical cyclogenesis in the western North Pacific*. NOAA,.

Zhang, Y., H. Wang, J. Sun, and H. Drange, 2010: Changes in the tropical cyclone genesis potential index over the western North Pacific in the SRES A2 scenario. *Advances in Atmospheric Sciences*, **27**, 1246–1258, https://doi.org/10.1007/s00376-010-9096-1.

Zhou, W., I. M. Held, and S. T. Garner, 2017: Tropical cyclones in rotating radiative–convective equilibrium with coupled sst. *Journal of the Atmospheric Sciences*, **74**, 879–892, https://doi.org/10.1175/JAS-D-16-0195.1.